

SANDIA REPORT

SAND97-8256 • UC-406

Unlimited Release

Printed April 1997

Predicting Weld Solidification Cracking Using Damage Mechanics - LDRD Summary Report

J. J. DIKE, J. A. BROOKS, D. J. BAMMANN, M. LI, J. S. KRAFCIK,
N.Y.C. YANG

Prepared by
Sandia National Laboratories
Albuquerque, New Mexico 87185 and Livermore, California 94551
for the United States Department of Energy
under Contract DE-AC04-94AL85000

Issued by Sandia National Laboratories, operated for the United States Department of Energy by Sandia Corporation.

NOTICE: This report was prepared as an account of work sponsored by an agency of the United States Government. Neither the United States Government nor any agency thereof, nor any of their employees, nor any of the contractors, subcontractors, or their employees, makes any warranty, express or implied, or assumes any legal liability or responsibility for the accuracy, completeness, or usefulness of any information, apparatus, product, or process disclosed, or represents that its use would not infringe privately owned rights. Reference herein to any specific commercial product, process, or service by trade name, trademark, manufacturer, or otherwise, does not necessarily constitute or imply its endorsement, recommendation, or favoring by the United States Government, any agency thereof or any of their contractors or subcontractors. The views and opinions expressed herein do not necessarily state or reflect those of the United States Government, any agency thereof, or any of their contractors or subcontractors.

Predicting Weld Solidification Cracking Using Damage Mechanics — LDRD Summary Report

J. J. Dike^{*}, J. A. Brooks[†], D. J. Bammann^{*}, M. Li[†],
J. S. Krafcik[†], N.Y.C. Yang^{**}

^{*} Mechanics & Simulation of Manufacturing Processes Department

[†] Advanced Manufacturing Technology for Metals Processing Department

^{**} Surface & Microstructure Research Department

Sandia National Laboratories

Livermore, California 94550

Abstract

This report summarizes the efforts to develop and validate a finite element based model to predict weld solidification cracking behavior. Such a model must capture the solidification behavior, the thermal behavior in the weld pool region, the material mechanical response, and some failure criteria to determine when solidification cracking will occur. For such a program to be successful, each aspect of the model had to be accurately modeled and verified since the output of one portion of the model served as the input to other portions of the model. A solidification model which includes dendrite tip and eutectic undercooling was developed and used in both the thermal and mechanical finite element analysis. High magnification video techniques were developed to measure strains for validation of the mechanical predictions using a strain rate and temperature dependent constitutive model. This model was coupled with a ductile void growth damage model and correlated with experimental observations to determine capabilities of predicting cracking response. A two phase (solid + liquid) material model was also developed that can be used to more accurately capture the mechanics of weld solidification cracking. In general, reasonable agreement was obtained between simulation and experiment for location of crack initiation and extent of cracking for 6061-T6 aluminum.

This page intentionally left blank

Table of Contents

Introduction	9
Solidification Cracking Mechanisms	9
Experiments	10
Materials	10
Solidification Behavior	10
Experimental Support for Validation of Thermal and Mechanical Finite Element Analyses of Welding	11
Testing and Cracking Response	12
Finite Element Simulations of Weld Solidification Cracking	13
Thermal Analyses	13
Solidification Model and Specific Heat	13
Thermal Conductivity	14
Heat Input and Thermal Losses	14
Finite Element Meshes	14
Comparison with Experiments	14
Mechanical Analyses	15
Parameters for the Constitutive and Damage Models	15
Damage Exponent	16
Elastic Constants	17
Selection of Time Step and Tolerance	17
Comparison of Strains Averaged Across the Weld	18
Analyses for Al-Cu Binary Alloys	18
Calculations of Crack Initiation	18
Requirements for Failure in the Solidification Region	21
Summary and Conclusions	22
References	24
Figures	26
Appendix A	42
Appendix B	45

List of Figures

Figure 1.	Schematic illustrating concept of hot strain during weld solidification versus material threshold strain for predicting solidification cracking from Matsuda, et. al.(2). Case (1) cracking, (2) marginal, (3) no cracking.	26
Figure 2.	(a) SEM microstructure of Al-Cu weld showing eutectic solidification product θ (CuAl_2) in interdendritic regions. (b) Measured and calculated dendrite core concentration and volume fraction of θ , in Al-Cu welds made at 12.7 mm/s.	26
Figure 3.	Predicted solidification behavior of Al- 5.93% Cu shown as concentration of solid vs fraction solidified.	27
Figure 4.	Fraction solid vs temperature for 6061 weld for solidification rate of 12.7 mm/s.	27
Figure 5.	Cracking specimens used for thermal/mechanical code validation (a) and cracking studies (b).	28
Figure 6.	Video images from underside of weld specimen. (a) weld coming into view at LHS (b) image taken after weld has passed. Strains are measured along position indicated.	28
Figure 7.	Schematic of Houldcroft solidification cracking specimen made from 0.050 inch thick sheet. Also noted on specimen is location of thermocouple placements.	29
Figure 8.	Solidification in weld cracking specimen in 6061. Note how crack initiates at outer edge of the fusion zone. Weld travels from right to left.	29
Figure 9.	(a) SEM image of region of solidification crack initiation, (b) higher magnification of crack surface showing eutectic solidification products.	30
Figure 10.	Properties used in thermal finite element analyses.	30
Figure 11.	Finite element mesh used in Houldcroft analyses.	31
Figure 12.	Finite element mesh used in analyses of 3"x6" slotted plates.	31

Figure 13.	Temperature comparison between analysis and experiment for Houldcroft specimen, 5.7 mm from weld centerline.	32
Figure 14.	Temperature comparison between analysis and experiment for Houldcroft specimen, 1.7 mm from weld centerline.	32
Figure 15.	Comparison of temperature histories for 55 A, 17 V, 12.7 mm/s GTA weld. CL refers to the weld centerline.	33
Figure 16.	Comparison of BCJ fit with data from (29) Strain rate 0.2 s^{-1} .	33
Figure 17.	Axisymmetric finite element mesh and boundary conditions used to determine damage exponent for elevated temperature notched tensile tests.	34
Figure 18.	Temperature dependence of damage exponent n in Equation 2 as determined by finite element fits to elevated temperature notched tensile tests.	34
Figure 19.	Temperature dependence of elastic constants used in mechanical analyses	35
Figure 20.	Stress-strain response for one-element mechanical analyses as a function of convergence tolerance at 400 C. 0.1%, 2%, and 10% tolerances.	35
Figure 21.	Stress-strain response for one-element mechanical analyses as a function of convergence tolerance at 400 C. 0.1%, 0.5%, and 2% tolerances.	36
Figure 22.	Comparison of transverse strains averaged across 6.35 mm weld for 6061-T6 Houldcroft specimen. Process parameters 40 A, 17V, 12.7 mm/s.	36
Figure 23.	Comparison of transverse strains averaged across 6.35 mm weld for 3"x6" slotted 6061-T6 specimen. Process parameters are 55A and 70A, 17V, 12.7 mm/s.	37
Figure 24.	Sample of disk specimen finite element model.	37
Figure 25.	Pressure, effective stress, and temperature as a function of time for an element at center of weld in disk specimen for modulus fit to compression data.	38

Figure 26.	Pressure, effective stress, and temperature as a function of time for an element at center of weld in disk specimen for single crystal elastic constants (32).	38
Figure 27.	Temperature at which pressure becomes tensile (<0) as a function of distance from weld start for disk specimen.	39
Figure 28.	Temperature at which pressure becomes tensile (<0) for elements spanning the weld near weld start for the disk specimen.	39
Figure 29.	Time histories of pressure for elements spanning weld near weld start.	40
Figure 30.	Effective stress as a function of temperature for elements spanning weld near weld start compared to yield stress as a function of temperature.	40
Figure 31.	Predicted cracking for test 1. Welds start at top of disk and proceed clockwise. Dark areas show failed elements.	41
Figure 32.	Calculated cracking for test 2, where cracking began near 190_ in the experiment.	41

List of Tables

Table 1.	BCJ constants used for mechanical analyses.	16
Table 2.	Weld process parameters for modeled disk tests.....	21
Table 3.	Locations at which through-thickness cracks initiate.....	21
Table 4.	Comparison of measured and calculated crack initiation locations for disk tests	22

Predicting Weld Solidification Cracking Using Damage Mechanics — LDRD Summary Report

Introduction

Weld solidification cracks are a common defect that can occur with all fusion welding processes. These cracks form during the later stages of solidification if sufficient stresses are developed to rupture the solid and liquid two phase structure. Solidification cracks can be extremely troublesome since it is difficult to quantify how close to the threshold between cracking and no cracking the welding process may be. Over the past 50 years many metallurgical investigations have been conducted to study cracking mechanisms and to determine effects of alloy compositions on cracking susceptibility (e.g. 1-3). Also many weldability tests have been developed to quantify compositional effects on cracking behavior (4, 5). In some cases test results may be related to production experience to determine if a problem may be anticipated and are especially useful when identical welds are produced using a number of heats of materials. However, when cracking does occur, the welding engineer is left to experience and intuition in developing a procedure or redesigning to eliminate these defects. Furthermore, when a weld of different geometry or constraint is produced, one may lack the production experience to predict weld cracking behavior. It has been recognized that additional tools are badly needed to deal with this often costly problem, one of these tools is computational modeling.

A successful computational model must accurately capture the solidification process, thermal and mechanical conditions in the weld region and material response. Recently, FEM analyses have been conducted to determine the importance of some of these factors (6-10). Furthermore, some failure criteria must be established to determine, given the above conditions, whether solidification cracking will occur. With such a model, one should have the ability to determine how to optimize the weld design and process to prevent the formation of solidification defects, and determine a priori whether or not solidification cracking will result. However, if one is to develop a FEM based solidification cracking model, extensive experimental validation of the different aspects of the model must be conducted to lend credibility to any model predictions. The work presented here summarizes different aspects of a weld solidification cracking model along with experimental validation conducted under an LDRD program.

Solidification Cracking Mechanisms

A number of theories have been developed to explain solidification cracking behavior (11, 12). In most all theories solidification cracking occurs during the final stages of solidification when a small amount of liquid is present. It is recognized that for cracking to occur one must have both a susceptible alloy composition and some degree of constraint. In the generalized theory of hot cracking developed by Borland (11), cracking occurs if there is insufficient solid boundaries to

withstand the applied stress during the final stages of solidification, or if insufficient liquid is present to backfill a crack if one initiates. Over the years slight modifications have been made to the original theory. For example, the relationships between the critical fraction of solid boundaries and amount of liquid is also dependent upon the relative solid/liquid surface energies.

Matsuda and co-workers (12) have related cracking susceptibility to the properties of the mushy zone by a region they term the brittle temperature region (BTR). This is a region they established using transverse restraint testing and measured cooling curves in the weld fusion zone. The temperature extends from the liquidus temperature to a temperature near the nonequilibrium solidus. Figure 1 summarizes the theory where cracking will occur if a critical strain is exceeded during the weld solidification process. However, the lower temperature of the BTR and the minimum critical strain may be dependent upon the amount of eutectic liquid, strain rate, and the grain structure for any given material. An important point to be made is that in this theory the factor considered to control cracking behavior is the strain with no mention of the nature of loading or stress state. In the more recent theories it has generally been considered that strain is a more critical factor than stress.

Experiments

Materials

The materials used in this study were Al- Cu binaries and the commercial aluminum alloy 6061-T6. The binary alloys were in the form of 50 mil sheet and 1/4" plate fabricated from five 9's pure starting material. The alloys consisted of 9 compositions ranging from pure Al to Al-7.7 wt% Cu. The 6061 was in the form of 1/4 inch plate.

Solidification Behavior

It is well established that a criteria for solidification cracks to form and propagate is the presence of small amounts of low melting liquids segregated to interdendritic and grain boundary regions during the last stages of solidification. To determine the fraction solid and liquid as a function of temperature one must have an accurate representation of the weld solidification behavior. This is also important in establishing the release of latent heat in the weld thermal model which affects the thermal fields in and around the solidifying weld region (9).

The Al-Cu binary alloys were used to develop and validate a solidification model that would accurately capture the solidification response during the weld process. The initial liquidus temperature, the volume fraction of solid and liquid as a function of temperature, and the final solidification temperature need to be captured. Al-Cu alloys exhibit eutectic solidification behavior, solidifying as primary Al with eutectic solidification occurring between Al - 5.65% Cu and CuAl_2 (θ). The equilibrium eutectic composition is 33 % Cu with a eutectic temperature of 548°C (13).

EB and GTA welds were made at 30 ipm (12.7 mm/s) in the different binary alloys to study the nonequilibrium solidification behavior. The concentration of the dendrite cores in the weld fusion zone were measured using electron microprobe analysis for the GTA welds and analytical electron microscopy for EB welds. From these measurements and the phase diagram, the degree of solidification undercooling can be determined. Here we assume there is insignificant solid state diffusion during weld solidification to change the concentration of the dendrite tip, which becomes the dendrite core, during the weld process. This assumption was verified in our solidification model incorporating diffusional effects. The volume fraction θ , as shown in the micrograph in Figure 2a, was measured using SEM images and an image analysis program. The experimental measurements were compared with theoretical predictions with the model incorporating both dendrite tip and eutectic undercooling. These results are shown in Figure 2b along with calculated and measured dendrite core concentrations. It can be seen that there is good agreement between the calculated dendrite tip concentration and measured dendrite core concentration when using the theory of Kurz, Giovanola and Trivedi, (KGT) (14). There is also good agreement between the measured and predicted volume fraction of θ .

The predicted solidification behavior of an alloy of Al - 5.93% Cu is shown in Figure 3 plotted as concentration of the solid vs fraction solidified. From the phase diagram the volume fraction solid vs temperature can now be calculated. The initial solidification temperature is decreased 15 K as a result of tip undercooling and a large fraction of solidification occurs early during the solidification process. The eutectic solidification temperature is also suppressed with a smaller fraction of eutectic solidification than is calculated assuming Scheil (15) behavior, also plotted in Figure 3. A similar type of analysis was used to calculate the solidification behavior of the aluminum alloy 6061.

The solidification behavior of 6061, primarily a Al-Mg-Si alloy, was treated as a pseudo binary system with a partitioning coefficient k (slope of the liquidus / slope of solidus curves), of 0.127. The equilibrium liquidus used was 928.8 K with the ternary eutectic temperature of 832.2 K. Both dendrite tip and eutectic undercooling were incorporated into the solidification analysis as discussed above. The tip undercooling was calculated to be ~ 6.2 K when using a KGT analysis with a solidification velocity of 30 ipm. Eutectic undercooling using the analysis of Jackson and Hunt (16) was calculated to be 6.7 K with the fraction eutectic solidification being 2.6 wt.%. Figure 4 shows the fraction of solid vs. temperature calculated using KGT model; this will be used in the weld thermal model to simulate the release of latent heat in the weld pool during cooling.

Experimental Support for Validation of Thermal and Mechanical Finite Element Analyses of Welding

An important aspect of the program was to validate finite element simulations of the welds. To do this weld pool shapes and weld thermal fields were measured. As discussed below, weld thermal response was measured in weld specimens using thermocouple arrays and a Keithly data acquisition system. As many as 15 thermocouples were used on each sample placed at different distances from the weld centerline. Comparisons between measured and calculated thermal profiles are discussed in the FEM analysis section.

A more challenging experimental task was to achieve some validation of the mechanical code, specifically strains occurring in the weld pool region during weld solidification and cooling. This was achieved using special lighting conditions and high magnification video images taken from the underside of the weld pool. Displacements were measured from digitized images of grid lines scribed on the underside of the sample (see Figure 5). Figure 6 shows a video image of the weld sample with the weld approaching from the left hand side of the image. The second image shows the same region of the sample after the weld had passed. By measuring the changes in grid spacing of many such video frames obtained during welding, strain histories could be calculated and compared to FEM predictions.

Another novel technique was investigated to measure strain in the HAZ during welding. The use of fiber optic sensors were investigated by Craig Lawrence and Tom Bennett (17). The sensors used are based on the Extrinsic Fabry-Perot Interferometer (EFPI), and were selected for their large measurement range, high resolution, short gage length, and ability to operate in high temperatures. This work showed considerable promise and is described in detail in Ref. 17. However, because of the success with the video technique in measuring strains in the fusion zone, and because of time constraints, comparisons between measured strains and FEM prediction were not made.

Testing and Cracking Response

A number of test specimens were used in this investigation. All specimens were designed to be self constraining during welding. Thus no external constraint or artificial loads or strains are applied during the test, and no external heat sinking was used which would cause uncertainty in the FEM boundary conditions. The test specimens were used to provide data to validate the FEM analysis and determine weld cracking behavior.

The first specimen investigated, utilizing 0.050 inch thick material, was the Houldcroft specimen shown in Figure 7. This commonly used specimen is designed with through thickness slots cut from the edge of the specimen to increasing distances toward the sample center. The weld is started at the edge of the sample with the shallow slots and extends the total length of the specimen. The increasing slot depth is intended to reduce constraint on the weld as the weld traverses the specimen. Parameters were developed that produced full penetration straight sided welds with a uniform width of ~3 mm. The weld parameters selected were 40 A DC , 17 volts, and 30 ipm (12.7 mm/s) weld speed using 100 % He shielding gas. In some cases Ar was used for back side shielding.

When using the Houldcroft test, it was found that the starting edge of the sample must be melted for a solidification crack to initiate and propagate. In general, the solidification cracking response of the Al-Cu alloys exhibited classic behavior. No cracking was observed in the pure Al. However, with increasing Cu content, cracking increased to a maximum value of 80% of the sample length at 2-3 % Cu, and then decreased to zero at the highest Cu level of 7.7%. When welding 6061-T6 material under the same conditions, the continuous centerline solidification crack extended ~80% of the sample length.

As discussed above, a crack in the Houldcroft test would initiate at the start of the weld and propagate along the weld centerline to a point to where it would abruptly terminate. We decided that for our work, it was better to attempt to predict crack initiation than crack arrest. This was partly due to expecting that the predictions of initiation would be more accurate than those of crack propagation. Therefore required the development of a different specimen geometry.

Two types of test specimens were designed using 1/4 inch thick material, one rectangular and one circular, shown in Figure 5. Both samples have a 1/2 inch wide slot producing a 0.050 inch thick web in which an autogeneous GTA weld was made. Arrays of up to 15 thermal couples were placed on the back side of the web of the rectangular specimens to measure temperature histories for validation of the FEM weld thermal model. As described earlier, grid patterns were also scribed on the back side of the rectangular plate which, along with video images, were used to measure displacements and thus strain behavior occurring during welding. The rectangular specimens were suspended on a three point fixture which allowed access for the underside video measurements and eliminated any external heat sinking or mechanical constraint. These specimens were used primarily to validate the thermal and mechanical code predictions.

A circular specimen shown in Figure 5b was used to determine the effect of welding conditions on weld cracking behavior and to correlate results with computational model predictions. These specimens were welded using a rotary fixture chucked to a pin placed in a 1/4 inch hole in the center of the sample, again to eliminate external constraint and heat sinking.

Samples were autogeneous GTA welded using a 3/32 or 1/16 inch diameter tungsten electrode with an arc voltage from 12V to 17V. Helium was used as the cover gas while Argon was used for back side shielding. Currents ranging from 30 to 120 amps and welding speeds of 10, 20 and 30 ipm produced straight sided full penetration welds. These specimens were welded using either one current level for the entire disc, or with three schedules where the starting current was increased at 120° and 240°. The extent of cracking was determined by viewing the top surface under a low magnification microscope.

The crack initiation region of a sample welded at 90 A is shown in Figure 8. In this sample the crack initiated at 90° from the weld start and followed the weld to completion at 360°. Figure 8 shows the intergranular crack initiated at the outer edge of the fusion zone and propagated to and along the weld centerline. This cracking behavior was common to most all the circular weld disc specimens. Many such specimens were run for comparison with code predictions.

The crack surfaces were examined with SEM and Scanning Auger Spectroscopy. SEM images are shown in Figure 9. Figure 9a shows, at low magnification, the region of crack initiation. On either side of the crack initiation region, dimples associated with ductile tearing during sample preparation are also apparent. The fracture surface in the region of initiation is shown at higher magnification in Figure 9b. Eutectic solidification products cover a fairly large region of the smooth dendritic appearing fracture surface. These surfaces are very characteristic of weld solidification cracks, although the detail of the development of the eutectic solidification products are somewhat unusual.

Based on the distinct appearance of the particles on the crack surface, one could conclude that a large fraction of the low melting eutectic liquid had solidified just prior to the fracture initiation process. However, the very smooth dendritic surface appearance indicates that solidification was not totally complete at the time of crack initiation. Still it is possible that fracture initiated in a region where some solid grain boundary regions existed with evidence of this fracture destroyed due to surface diffusion at the very high temperatures. However, it should be noted that all regions of the fracture surface looked similar with no apparent region of fracture occurring in the solid. Thus we have concluded that fracture initiated in the lower temperature region of the brittle temperature range near the eutectic temperature.

Finite Element Simulations of Weld Solidification Cracking

Thermal Analyses

Solidification Model and Specific Heat

The thermal analysis process is described in (6,9,18,19). The Sandia finite element thermal code JACQ3D (33) was used to perform the analyses. The High Temperature Materials Information Analysis Center (20) was contracted to provide recommended values of the thermal properties from room temperature to melt. The solidification model was used to generate the fraction solid as a function of temperature curve for the alloy of interest based on an equilibrium phase diagram and the welding speed. For 6061-T6, a pseudo-binary diagram discussed in (9) was used. For the Al-Cu binaries the Al-Cu phase diagram was used along with previously described solidification model. This curve was differentiated to obtain the rate of solidification as a function of temperature. The latent heat of fusion was then added to the baseline specific heat curve to match the rate of solidification. The result was a very nonlinear specific heat curve as shown in Figure 10. Figure 10 shows a spike at the eutectic temperature (approximately 828 K) and a large spike near the liquidus temperature at 920-930 K for 6061-T6 Al for a 30 inch/minute (ipm) weld. The flat region at the liquidus shows the temperature region over which the solidification at the liquidus temperature was spread. This nonlinearity would often cause numerical difficulties resulting in lack of convergence in JACQ3D. The large nonlinearities in the specific heat were due to significant fractions of the material solidifying at a constant temperature. As can be observed in the solidification model's predictions of fraction solid as a function of temperature (Fig. 4) solidification occurs very rapidly near the liquidus temperature, with approximately 50% solidifying within a few degrees of the liquidus temperature, and 80% solidified within 10 K of the liquidus. The solidification range was nearly 100 K with about 3% eutectic solidification for many of the 6061-T6 analyses. Thus in the analyses a large peak in the specific heat curve is required to simulate the solidification rate. References (6) and (21) showed how different solidification models could affect isotherm shapes near the weld pool. In particular, it was shown how isotherms were elongated near the tail of the pool in the solidification temperature range when a more realistic solidification model was used. As the weld pool is surrounded by a compressive stress and followed by tensile transverse stress, anything that causes the weld pool to become elongated may increase the chance of solidification cracking. The susceptible material may be pushed closer to the trailing tensile region. Reference

(6) also showed how the solidifying region changes in a thermal analysis based on the assumptions of the solidification model.

In (6), different thermal properties were used on-heating and on-cooling. The lever rule was used to determine the melting rate and then Scheil behavior was used for solidification. Implementing this into the finite element analyses required modifying the code to use different properties on-heating and on-cooling. However, it was determined that melting occurs much more quickly than solidification in these problems. Using the same properties for melting and solidifying simplifies the problem without appearing to significantly alter the thermomechanical response during solidification. This was the technique used for the majority of the analyses.

Thermal Conductivity

Figure 10 also shows the thermal conductivity increasing by a factor of 4 at the liquidus temperature. The conductivity is modified in this manner to account for enhanced convection that occurs in the weld pool due to stirring and digging of the welding arc. The multiplication factor is based on studies of fluid mechanics and heat transfer in the weld pool (22).

Heat Input and Thermal Losses

Energy was input to the thermal model using a double ellipsoidal volumetric heat source (23). Dimensions for the heat source model came from measurements of weld ripples (pool profile) and fusion zone cross-sections. Heat input efficiencies between 70% and 80% were adjusted to match thermocouple histories. Thermal losses were accounted for by combined radiative and free convection heat transfer being combined into a temperature dependent effective convective heat transfer coefficient. Often the radiative and convective heat loss mechanisms did not play an important role in the thermal response because the times involved were relative small (typically 8 to 30 s). During this time span conduction within the specimen largely controlled the thermal response.

Finite Element Meshes

Meshes used for validated thermal analyses are shown in Figures 11 and 12 for the Houldcroft and 3"x6" specimens, respectively. Figure 11 shows the Houldcroft mesh constructed of approximately 13,000 8-node hex elements. Various meshes were used throughout the analyses to evaluate mesh dependence. Typically the mesh had at least 4 to 5 elements across the width and length of the weld pool. Ideally, at least this many elements is desired along the mushy zone to capture the temperature and stress gradients in the solidifying material. Figure 12 shows the mesh used for the 3"x6" slotted specimen. It is constructed of approximately 32,000 8-node hex elements.

Comparison with Experiments

Schematics showing the locations of the TC's are shown in Figures 6 and 7. Examples of temperature comparisons are shown in Figures 13, 14, and 15. Figures 13 and 14 show temperature histories for a Houldcroft test 5.7 and 1.7 mm from the weld centerline, respectively. There are six thermocouple histories shifted in time to overlay each other so that the scatter can be observed. The analysis history is also shown by the line with symbols. Nearer to the weld centerline (Fig. 14) there is more scatter in the experimental data. This may be due largely to

uncertainties in the position of the thermocouple relative to the weld centerline. As positions closer to the weld centerline are examined, the histories will be more sensitive to uncertainties in location due to the increasing steepness of the temperature gradient. The calculated temperature in Figure 14 is somewhat high, but overall agrees well with the experimental data

Figure 15 shows a comparison of temperatures from the finite element analysis and an experiment using the 3"x6" rectangular plate. Thermocouple locations on opposite sides of the weld are indicated by solid or open symbols. The data shows that the thermocouples did not end up being equally spaced away from the weld centerline, perhaps due to misalignment of the specimen with the torch travel direction. The analysis curves are at the nominal locations specified in the thermocouple schematic, Figure 5a. The results in Figure 15 indicate that the analysis compares well with the test, as the calculated temperature histories fall between the experimental curves. There is a difference in the curve shape at the location closest to the weld centerline. The analysis curve is significantly wider than the thermocouple history from the peak temperature of approximately 1100 K (liquidus temperature is approximately 928 K) to 600 K. There was only one thermocouple that survived at this location, so it is not clear how much scatter there is in the data. The peak temperatures do agree well. It was determined that overall, the thermal analyses were sufficiently accurate to proceed to the mechanical analyses. There are still many details that could be improved in matching analysis to experimental thermal data, but it was believed that the first order effects had been captured in the finite element model.

Mechanical Analyses

Parameters for the Constitutive and Damage Models

Two versions of the Bammann-Chiesa-Johnson (BCJ) plasticity and damage model were used (24-27) in the mechanical finite element analysis code JAS3D (33,34). The majority of analyses used the single phase model which is described in Appendix A. A few preliminary analyses used the two-phase (liquid+solid) version of the BCJ model, which is described briefly in Appendix B. It was developed and integrated into the mechanical code JAS3D but time was not available to test the model.

The BCJ plasticity model has 20 parameters, while the damage model requires one additional parameter. The software BFIT (28), a nonlinear least squares package specifically designed to fit parameters to the BCJ model, was used to generate parameter sets based on available data. Strain rate and temperature dependent stress-strain responses for 6061-T6 from room temperature to melt were not readily available. Initially information at small strains and relatively low temperatures was extrapolated to melt and beyond. Near the end of the project additional data from the National Center for Excellence in Metalworking Technology (NCEMT) was obtained, but there was not time to integrate the information into the analyses. Also near the end of the project, we were able to perform a limited number of compression and notched tensile tests (29). A subset of this data was used to generate the fit shown in Figure 16. The BCJ parameters used are listed in Table 1. Units for the parameters are MPa, K, s.

Table 1. BCJ constants used for mechanical analyses, MPa, K, s units.

Parameter	Value	Parameter	Value
C1	0	C11	0.001454
C2	0	C12	252.1
C3	37.68	C13	2.073e5
C4	630	C14	6394
C5	1e-5	C15	67.77
C6	0	C16	0.06024
C7	32.62	C17	3.913e-3
C8	1434	C18	2468
C9	937.1	C19	0.017
C10	1.236	C20	770

Damage Exponent

The evolution of the damage parameter ϕ is given by

$$\dot{\phi} = \beta \left[\frac{1}{(1-\phi)^n} - (1-\phi) \right] |D^p| \quad (1)$$

where $|D^p|$ is the magnitude of the deviatoric plastic stretch and β is a function of the stress triaxiality (pressure/effective stress) and the damage exponent n . The exponent n in (1) controls the rate at which voids grow for a given level of stress triaxiality. Tests were conducted (29) to obtain a rough estimate of how the damage exponent n varies with temperature. Typically, notched tensile specimens with different ratios of the notch radius to the minimum specimen diameter are used to introduce various levels of triaxiality into the gage section of the specimen. Trial and error finite element analyses are used to determine the damage exponent once parameters for the plasticity model have been determined from separate compression tests. In this work, a limited number of tests were performed to study the temperature dependence of n for 6061-T6 aluminum. Tests were performed at 23 C, 300 C, and 400 C. Specimens were induction heated rapidly then held for 60 s at temperature. The specimens were then pulled and force-displacement data was collected. The hold times are longer than those experienced during welding. However, the tests still provide an estimate of how the damage exponent varies with temperature. An axisymmetric finite element model of the specimen used in the tests is shown in Figure 17. Figure 17 also indicates the boundary conditions applied to the model to apply the appropriate symmetry and loading conditions.

The temperature dependence of the damage exponent n as determined through trial and error finite element analyses of the elevated temperature notched tensile specimens is shown in Figure 18. Using the three data points and an estimated saturation level, a hyperbolic tangent shape is assumed for n as a function of temperature, as shown in Eqn. 2.

$$n(T) = n_s + (n_o - n_s) \{ 1 + \tanh [(C_1 - T)/C_2] \} / 2, \quad (2)$$

where T is temperature, n_o is the room temperature value, n_s is the saturation value, and C_1 and C_2 are constants fit to the data. The parameter values are listed in Figure 18. From extensive data in

the literature it is known that cracks do not form in the weld pool itself, but rather in the mushy zone, where the partially solidified material exists, or in regions recently solidified. For this reason a saturation value of 0.6 was assumed. At $n=0.5$, damage does not increase in the formulation implemented in the BCJ model. Because the hyperbolic tangent curve is fairly flat by the liquidus temp (~ 828 K here), the saturation value of 0.6 was selected to allow failure in the solidification temperature range.

The constitutive model subroutine was modified such that damage increased only in elements that were below a temperature termed the coherent temperature. The coherent temperature was determined from the solidification model as the temperature at which the material was 75% solidified. This is approximately when the material is able to carry a tensile load due to the dendrites forming an interconnecting network (30,31). In addition, if the element temperature was above the solidus temperature, damage was only allowed to increase if the element was resolidifying - this prevented material failing as it melted.

There is still a large degree of uncertainty in the shape of the curve due to using only three data points and an assumed saturation level, but the information should be an improvement over assuming a constant value for the parameter. It was observed in the tests that the force-displacement curves were strain rate and temperature history dependent, but no attempt was made to include these factors into the damage exponent's evolution. In separate single-element analyses looking at the effect of time to failure as a function of n , it was observed that for a given set of boundary conditions, the time to failure as a function of n was relatively independent of temperature. This seems reasonable since the triaxiality is independent of temperature for this case. The trend in time to failure as a function of n appeared to be linear. This information was used in some of the mechanical analyses to ascertain what was the factor driving cracking

Elastic Constants

Two different sets of elastic constants were used because it was not clear which was more appropriate to use in the analyses. Measurements of single crystal elastic constants in aluminum (32) from room temperature to melt were used to generate one set of constants. Their data was used assuming C_{44} = the shear modulus and C_{12} = Lamé's constant. The data implies Young's modulus decreasing linearly from room temperature to melt, decreasing to approximately 63% of the room temperature value at melt. Similarly, using the elastic constants to calculate Poisson's ratio produces a linear increase at melt of about 14% over the room temperature value. Both curves were linearly extrapolated for temperatures above melt.

When these curves, in particular the curve for Young's modulus, were used in generating the fit to the BCJ model based on data in (29), it was observed that a much better fit to the apparently elastic portion of the compression data was obtained using much greater temperature dependence than observed in (32). Based on knowledge of the room temperature value of the modulus and fitting the linear portions of the compression data, a hyperbolic tangent function was fit to Young's modulus. This curve and the Poisson's ratio curve generated using data in (32) composed the second set of elastic constants considered. The resulting curves are shown in Fig. 19.

Selection of Time Step and Tolerance

The dynamic relaxation (DR) solution type was used for almost all of the mechanical analyses because it appeared significantly more robust than the conjugate gradient (CG) algorithm. The DR run times were usually greater than those of the CG runs, often by about a factor of 3. However, convergence appeared much more independent of step size, tolerance, and mesh than it did in the CG runs. It was observed that tighter tolerances seemed to be required for the DR runs to match stress histories produced using the CG method.

Single-element analyses were performed with the BCJ fit described above to determine the effect of convergence tolerance. Relative tolerance values (residual norm / applied force norm) were varied from 10% to 0.1%. Engineering strains of 20% were generated using a prescribed velocity and 10, 100, and 1000 time steps during the loading. Figures 20 and 21 show the results at 400 C. Similar trends were observed at room temperature and 828 K. With a 2% tolerance, the stresses differed from the 0.1% values by up to ~6%. A tolerance of 2% produced results within 1% of the 0.1% tolerance results. Reducing the time step to give 1000 steps over 20% strain with a 0.1% tolerance produced results nearly identical to the 100 step case. Reducing the number of time steps to 10 in the 2% tolerance analysis showed a strain at yield of about 2% versus 1% when 100 steps were used. Based on these results, tolerances of 2% were typically used in the weld simulation analyses. Several welding simulations were performed using tolerances of 2% and 0.1% to make sure the 2% value was adequate. The analyses produced very similar stress histories and cracking predictions.

Time steps were selected to produce several data points through the solidification range when crack initiation was of interest. This choice resulted in time steps of approximately 0.035 s. When strains averaged across the weld were the item of interest, larger time steps (~ 0.2 s) could be taken without significantly altering the predicted strains.

Comparisons of Strains Averaged Across the Weld

The rectangular specimens (Houldcroft and 3"x6" grooved plate) were used to validate temperatures and strains calculated in the analyses. Figure 22 shows strain histories for a Houldcroft test in which the specimen did not crack compared with analysis. As described in the Experimental section, video techniques were used to generate strain histories. Here the gage length is approximate 6.35 mm. This was one of the first mechanical analyses and a bilinear constitutive model was used rather than the BCJ. The resolution of the video technique was approximately 0.2%.

Figure 23 shows strain history comparisons for two 3"x6" plates that did not crack. Two current levels were used and strains were measured at different locations. The locations are shown by the video strain grids in Fig. 7a. Analysis results compare well with the strain histories. Gage length is again approximately 6.35 mm.

Analyses for Al-Cu Binary Alloys

A limited number of thermal and mechanical analyses were performed for the Al-Cu binary alloys. Although the phase diagram and solidification behavior is better understood for these alloys, there is not as much mechanical or thermal property data available from room temperature

to melt as for 6061-T6. A significant amount of stress-strain response data was generated during the project using the Gleeble testing machine, but some questions of interpretation and limited time and resources prevented the results from being integrated into any of the finite element analyses. It also appeared that additional failure criteria would be required in the BCJ model to account for the alloy dependence of weld cracking susceptibility observed in experiments. Therefore effort was focused on simulating welds on 6061-T6 samples.

Calculations of Crack Initiation

Calculations of thermal and mechanical responses were verified, at least in a general sense, using the rectangular specimens. The Houldcroft specimen was not used for validating cracking calculations because it was more a test of crack extension rather than crack initiation. It was believed that finite element predictions of crack initiation are more reliable than predictions of crack extent, and crack initiation is really of more interest at this time. Therefore a test in which crack initiation varied with load was sought. The circular patch test was found to be useful for studying crack initiation. Several finite element meshes of the specimen were generated, with a representative mesh presented in Figure 24. It was constructed of approximately 8500 8-node hex elements. One to three elements were used through the web thickness. The disk appeared to remain flat during the experiment and the majority of welds were full penetration with fusion zone boundaries perpendicular to the web surface, so capturing bending stresses was not a major concern. Typical run times for the thermal analyses were approximately two hours on a Cray J90. Mechanical analyses averaged approximately 5 hours for a 2% tolerance, 0.2 s step size (32 s weld) to approximately 50 hours for 0.05% tolerance, 0.035 s step size.

Many analyses were performed to study the relationship between stress, temperature, and damage for an experiment in which the crack formed very near the start of the weld. Because the material response near melt is not well characterized, analyses were performed to determine how the choice of elastic constant, damage exponent, and thermal expansion behaviors near melt affected the items listed above.

Figure 25 shows the pressure, von Mises stress, and temperature history for an element near the start of the weld at the weld centerline. It shows the effective stress going very close to zero during the time the material is melted. The effective stress then rises smoothly as the temperature drops below the solidus temperature. Figure 25 was generated using the Young's modulus curve that was matched to compression test data. Figure 26 shows the same data using Young's modulus calculated from the elastic constant measurements in (32). It shows the effective stress remaining close to zero longer than when the modulus gets very small at melt (shown in Fig. 25). Figure 26 also shows the pressure becoming tensile (negative here) sooner than in Fig. 25. This implies that failure is likely to occur sooner when a modulus that remains relatively large at high temperatures is used than when a modulus that tends to zero at melt is used. However, the curve generated using the high high-temperature modulus is not as smooth as that for the low high-temperature modulus. This may indicate a tighter tolerance should be used or that this set of elastic constants is somewhat more difficult to handle numerically than the set obtained by fitting the slopes of the compression test data.

The pressure becomes tensile (negative here) in Fig. 25 near 550 K, well below the solidus temperature. As the rate of energy input is increased into the part, for instance by increasing the current and keeping other quantities the same, the temperature at which the pressure becomes tensile increases. For instance, increasing the current by 35% causes the temperature at which the pressure at the weld centerline becomes tensile to increase by more than 50 K. Other factors such as the temperature dependence of the elastic constants and the yield strength influence when the pressure becomes tensile. The tensile pressure crossover temperature (where it becomes tensile during solidification) increases as the elastic modulus is increased. The thermal expansion temperature dependence also influences this tensile pressure crossover. More expansion appears to push the tensile region closer to the weld pool, however it also makes the pressure histories much noisier in the analyses. It was also observed that when the yield strength is increased in the solidification range, the tensile pressure crossover temperature increased. The interaction of these affects still needs to be determined, and it is apparent that to quantitatively predict solidification cracking, material properties near melt must be better defined. Also not included in any of the modeling are effects of grain size and microstructure, which are known to influence material properties.

It was observed in the experiments that once the cracks started they continued to follow the weld to the end of the test. To understand part of the reason for this, histories of pressure/effective stress were compared for elements on the weld centerline at different positions along the disk welds. This analysis did not allow cracks to form. Figure 27 shows these histories for elements 0, 90, 180, and 270 from the start of the weld. The pressure/effective stress ratios are plotted against temperature for each element to compare when the pressure becomes tensile with respect to the element temperature. Figure 27 shows that the temperature at which the pressure becomes tensile increases as the weld proceeds - indicating that the likelihood of solidification cracking increases at greater distances from the weld start. This is partly due to the overall temperature of the part increasing as the weld progresses and the contraction of all the elements previously welded. It can also be observed from Figure 27 that the pressure/effective stress is relatively constant for a period after the weld pool passes. It is also of interest to note that the ratio is relatively independent of position around the weld, at least for the modeling assumptions used here. This indicates that the loading does not necessarily increase with distance from the weld, but rather that the tensile loading appears to develop in material more susceptible to cracking as the torch travels around the disk.

It was also observed in the disk experiments that cracks usually initiated on the edge of the weld farthest from the disk center, as shown in the close-up in Figure 8. The finite element analyses provide some indication of why this occurs. Figure 28 shows pressure /effective stress ratios as a function of temperature for five elements spanning the weld at a location close to the start of the weld. Element A is closest to the center of the disk and is at the inner edge of the weld. Element E is at the edge of the weld closest to the outer edge of the disk. Elements B, C, and D are equally spaced between A and E, with element C being at the weld centerline. Figure 28 shows that with respect to temperature, the pressure becomes tensile first at the inner and outer edges of the weld. This may partially explain why cracks initiate on the outer edge of the weld. The centermost element is loaded by a tensile pressure last. Again all of the locations show about the same level of triaxiality (pressure/effective stress). In Figure 28 it appears that the innermost element actually sees tensile loads slightly earlier temperature-wise than the outer element.

Figure 29 shows time histories of pressure for the five elements. This figure indicates that the outermost element is subjected to the tensile load earlier in time than the innermost element. This would suggest the outer element should fail first even though the innermost element is loaded in tension at a higher temperature. Failure of the outermost element will relieve some of the load so the inner element would be less likely to fail. This is consistent with the behavior observed in the experiments.

Another indication that the outer edges of the weld are more likely to be crack initiation sites than the center is that the temperature at which the stress drops below the local yield stress occurs last at the outer elements. This would indicate that material is plastically deforming during solidification longer in elements at the weld edge than at the weld center. This is shown in Figure 30. The yield stress is shown to drop from approximately 10 MPa at the nonequilibrium solidus temperature of 828 K to approximately 0.6 MPa at the liquidus temperature of 928 K. Forest and Bercovici (30) and Nedreberg (35) both discuss test data for yield strength near melt indicating yield strengths at the solidus temperature for aluminum alloys on the order of a few MPa. The yield stress drops to zero between 75% and 85% fraction solid in (30). Figure 30 indicates that effective stress in the center element C in the weld drops below the yield stress near 870 K in this example. In the two elements just off-center, the effective stress drops below yield near 865 K. Finally, in the elements at the weld edges the effective stress drops below yield near 835 K. The actual temperatures at which this occurs are probably not well predicted, but the trend appears to be consistent with the experimental observations of crack initiation.

Simulations of the four tests described in Tables 2 and 3 were performed to determine where cracking would initiate. Figure 31 shows predicted cracking for test 1 in which a continuous crack formed near the start of the weld at ~0_. Welding begins at the top of the figure and proceeds clockwise. The dark areas show failed elements which represent cracks. Figure 31 shows some cracking is predicted on both sides of the weld, but more failure occurs on the outside edge of the weld. This is somewhat consistent with the observations of cracks initiating on the outer edge of the weld. Cracking is not predicted to go to the weld centerline, rather it stays on the outer edges of the weld. One explanation for this is that no information is included in the model regarding grain orientation or any directionality or property changes due to the microstructure. In addition, the discretization of the model may not be sufficient to capture the crack extension correctly. Rather it appears more as a continuous series of initiations. Another observation is the failures are discontinuous at first. This is due partly to the tolerances used in the analyses. Tighter tolerances produce less of the discontinuous failures but essentially reproduce the failure shown in Figs. 31 and 32, though at significantly greater computational expense. It also was observed in experiments on similar geometry specimens in Al-Cu alloys that for some conditions many cracks would initiate but not propagate early in the weld.

Table 2. Weld process parameters for modeled disk tests.

Test	current (A)			travel speed (mm/s)
	position around disk			
	0_-120_	120_-240_	240_-360_	
1	50	55	60	6.35
2	30	40	50	6.35
3	60	70	80	10.7
4	40	50	60	10.7

Table 3. Locations at which through-thickness cracks initiate.

Test	crack initiation (distance from weld start)
1	0_
2	190_
3	0_
4	160_

The same modeling assumptions and procedures were applied to the other three disk tests. Figure 32 shows calculated cracking for test 2, in which cracking began at 190_ in the experiment. The analysis shows failure beginning near 130_ with a continuous crack beginning near 165_. Table 4 lists the results for the analyses corresponding to the four disk tests described in Table 3. Failure in the simulations is presented by listing the angles at which a continuous crack forms. Analyses with higher resolution, spatially and perhaps temporally, would provide a more definitive estimate of when cracking initiates using the current damage model. Another consideration in comparing the calculated and experimental results is that a limited number of experiments were performed, so the scatter in the experiments is not known. The main objective was to demonstrate the correct trends, and if the models are calibrated to a test, they do seem to be useful in predicting trends for other process parameter sets and geometries. The same modeling assumptions were used on the rectangular plates in which no damage was observed in the tests. No failure was predicted in the models.

Requirements for Failure in the Solidification Region

In the context of the BCJ model and the void growth damage model, three requirements must be satisfied simultaneously to cause an element to fail in the solidification region. The first requirement is the hydrostatic pressure must become tensile somewhere in the solidifying material. Without a tensile pressure there is no driving force for void growth. If the hydrostatic

pressure is not tensile, β in Eqn. 1 is zero, resulting in zero rate of change in damage. The second requirement is that the material be plastically deforming while a tensile pressure exists, since void growth occurs only during plastic deformation in the model. The third requirement is that the level of triaxiality, or the ratio of the pressure over the effective stress (p/σ_{eff}), be large enough to drive the void growth to failure. For a given value of p/σ_{eff} , the damage exponent in Eqns. 1 and 2 must be large enough to cause damage to increase to the failure level during the time the three requirements above are satisfied.

Table 4. Comparison of measured and calculated crack initiation locations for disk tests.

Test	location of crack initiation (distance from weld start)	
	experiment	model
1	0_	0_
2	190_	165_
3	0_	5_
4	160_	130_

Summary and Conclusions

The weld cracking susceptibility were used to validate finite element simulations of the welding process. Tests using specimens with rectangular geometries were used for validating calculations of temperatures and strains averaged across the welds. The circular patch test specimens were used to validate calculations of crack initiation.

The solidification model was incorporated into the finite element simulations, mainly through modification of material properties in the solidification temperature range. In the thermal analyses the solidification model was used to modify the specific heat curve to correctly represent the rate of solidification. The mechanical analyses used the solidification model's results to modify damage behavior and, for the two-phase BCJ model, determine the effective behavior of an element in which fluid and solid phases coexisted.

The finite element simulations were largely successful at modeling the thermal and mechanical responses observed in the experiments. Temperature histories near the weld pools as measured by thermocouples were simulated well in the analyses. Some details of the weld pool shape were not captured. However, it is not known at this point the importance of these details. Calculations of strains averaged across the approximately 0.25" wide welds agreed well with strains measured by video techniques in the experiments. No information as to how accurately stresses were calculated is available. Some idea of how accurately stresses were calculated might be obtained using neutron or x-ray diffraction techniques even at room temperature, though the resolution and accuracy in the center of the weld might not be high enough to be useful.

Predictions of solidification cracking were partially successful. It does appear that cracking trends as a function of load situation are available using the analysis techniques employed here.

For instance, it appears that it may be possible to determine which one of a number of processes or restraint systems to which a particular specimen is subjected is the most likely to cause cracking. Similarly, the effect of part geometry and weld groove geometry may be determined. However, we do not currently have a model that could determine the solidification cracking trends as a function of material or alloy (e.g. %Cu in Al-Cu alloys). Also, considerable effort needs to be devoted to understanding and modeling damage evolution and failure at high temperatures to be able to generate accurate quantitative predictions of solidification cracking.

The problem is very difficult for several reasons. One is that cracking occurs at high temperatures, where material properties are poorly defined even for static load situations. The situation is even worse when temperature history, strain rate, and microstructural effects are involved. Modeling failure at high temperatures is not well developed. For instance, it is not well understood how the damage model integrated with the BCJ plasticity model should behave at high temperatures. With regards to the finite element models, some of the thermal properties used in the analyses are very nonlinear which can cause numerical difficulties in the codes. Softening of the materials in the mechanical analyses can also cause numerical difficulties. The fact that solidification can occur over a very small temperature range makes it important to use small time steps to capture the response accurately, making computer cpu run times large. The need for adequate spatial resolution in the finite element model to capture temperature and stress gradients near the weld pool and mushy zone where cracking occurs also adds to the demand for computational resources.

Conditions for failure in terms of an internal state variable plasticity model coupled with a ductile void growth damage model were discussed with reference to solidification cracking. In order for solidification cracking to occur three conditions must be satisfied during solidification. (1) The solidifying material must experience a tensile hydrostatic stress, (2) the material must be deforming plastically for voids to grow, (3) the ratio of the hydrostatic stress / effective stress must be sufficiently large for the voids to grow fast enough such that failure occurs before the material cools significantly below the local solidus temperature.

It was observed in the analyses that the temperature at which the pressure behind the weld pool becomes tensile increases with stiffer elastic constants, higher yield strength, increased power input, and for the disk specimen, distance from the weld start. It was observed that the magnitude of the triaxiality (pressure/effective stress) does not appear to significantly increase with location around the disk. The likelihood of cracking increases with distance from the weld in the disk specimen because the temperature at which the pressure behind the pool becomes tensile increases. The effect of this is that material more susceptible to cracking is loaded by the tensile pressure as the weld proceeds around the disk.

The thermomechanical conditions responsible for causing crack initiation on the outside edge of the weld fusion zone in the disk specimens were explained by noting that at the outer edges of the weld tensile pressures develop at higher temperatures than at the weld center. The outer edge cracks rather than the inner edge because the outer edge sees the tensile pressure earlier in time than the inner edge. Further, under the assumptions used in this work, the outermost elements under go plastic deformation over a larger temperature range than the center elements.

Finally, four disk tests were simulated and calculated crack initiation locations bounded those observed in the experiments. However, the observed centerline cracking was not predicted.

We believe that in a fairly short period of time, 2 years, we have laid a strong foundation for modeling weld solidification cracking behavior. With additional time and effort, we believe we can develop a very powerful and useful tool for many weld applications. Future work would focus on including more information about the microstructure and better defining the mechanical properties near melt. It is also important to extend the modeling techniques to capture alloy dependence of solidification cracking. Improvements in the model to predict the weld centerline cracks observed in the experiments is another goal, which would utilize microstructural modeling.

References

1. Borland, J. C., and Younger, R. M., "Some Aspects of Cracking in Welded Cr-Ni Austenitic Steels". British Welding Journal (7), 1960, 22-59.
2. Medovar, I., "On the Nature of Weld Cracking", Translated from *Artomaticheskaya Svarka* 7 (4) 1954, 12-28.
3. Apblett, W. R., and Pellini, W. S., "Factors which Influence Weld Cracking", *Welding J.* 1954, 33(2), 83s-90s.
4. Vagi, J. J., Meister, R. P., and Randal, M. D., "Weldment Evaluation Methods", DMIC Report 244, August, 1968.
5. Campbell, R. D. and Walsh, D. W., "Weldability Testing", in *ASM Handbook*, Vol. 6, Welding, Brazing and Soldering, ASM International, 1993 603-613.
6. Brooks, J.A., Dike, J.J., and Krafcik, J.S., "On Modeling Weld Solidification Cracking", *International Conference Proceedings on Modeling and Control of Joining Processes*, Orlando FL, 1993, p. 174-185.
7. Feng, Z. and Tsai, C. L., "Modeling of Thermal Mechanical Conditions at Weld Pool", *International Conference Proceedings on Modeling and Control of Joining Processes*, Orlando FL, 1993, p. 525-532.
8. Zacharia, T., "Dynamic stresses in weld metal hot cracking", *Weld. J.* vol.73 (7), p. 164-s to 172-s.
9. Dike, J. J., Brooks, J. A., and Krafcik, J. S., "Finite Element Modeling and Verification of Thermal-Mechanical Behavior in the Weld Pool Region", *Proc. 4th International Conference on Trends in Welding Research*, Gatlinburg, TN, June, 1995, Ed. H. B. Smartt, J. A. Johnson, S. A. David, 159-164.
10. Feng, Z., Zacharia, T., and David, S.A., "Modeling of Thermomechanical Conditions in the Sigmajig Weldability Test", *Proc. 4th International Conference on Trends in Welding Research*, Gatlinburg, TN, June 1995, ed. H. B. Smart, J. A. Johnson, and S. A. David. 621-626.
11. Borland, J. C., "Generalized Theory of Super-solidus Cracking in Welds", *British Welding Journal* 7(8):1960, 508-512.
12. Matsuda, F., Nakagawa, H., and Sorado, K., "Dynamic Observation of Solidification and Solidification Cracking during Welding with Optical Microscope (I) - Solidification Front and Behavior of Cracking", 1982, *Trans. JWRI*, 11 (2), 67-77.
13. Massalski, T. B., *Binary Alloy Phase Diagram*, second edition, ASM International, 1990.
14. Kurz, W., Giovanola, K B., and Trivedi, R., *Acta Metall.*, 1986, 109-116.
15. E. Scheil, *Z. Metallk.* 34:70, 1942
16. Jackson, K. A. and Hunt, J. D., *Trans. AIME*, vol. 36, 1966, 1129-42.
17. Lawrence, C. M., Bennett, T.E., "Measurement of Process-induced Strains During Welding with Fiber Optic Sensors", memo Oct 24, 1996.
18. Dike, J. J., Brooks, J. A., Bammann, D. J., and Li, M., "Thermal-Mechanical Modeling and Experimental Validation of Weld Solidification Cracking in 6061-T6 Aluminum", *Proc. of ASM Int'l European Conf. on Welding and Joining Science and Technology*, Madrid, Spain, March 10-12, 1997.
19. Dike, J. J., Brooks, J. A., Bammann, D. J., Li, M., Krafcik, J. S "Finite Element Modeling of Weld Solidification Cracking in 6061-T6 Aluminum - Applicability of

- Strain-based Failure Criteria”, to appear in Proc. of International Symposium on Thermal Stresses and Related Topics, Thermal Stresses ‘97, Rochester, NY, June 8-11, 1997.
20. Desai, P. D., Gilp, B. F., Cooney, J. S., and Bogaard, R. H., “Thermophysical and Mechanical Properties of 6061-T6 and 6061-O Aluminum Alloy from Room Temperature to Melt”, MIAC Special Report 7, Center for Information and Numerical Data Analysis and Synthesis, Purdue University, West Lafayette, IN, March, 1995.
 21. Feng, Z., 1993, “A Methodology for Quantifying the Thermal and Mechanical Conditions for Weld Solidification Cracking”, Ph.D. Dissertation, Ohio State University.
 22. Kanouff, M. P., “The Effective Thermal Conductivity in Weld Pools”, Internal Sandia Memo, April, 1994.
 23. Goldak, J., Chakravarti, A., and Bibby, M., “A New Finite Element Model for Welding Heat Sources”, Met. Trans. B, 15B, pp. 299-305, 1984.
 24. Bammann, D. J., “An Internal State Variable Model of Viscoplasticity” in Media with Microstructures and Wave Propagation, Afantis, E. and Davison, L. eds., Int. J. Eng. Sci., Vol. 8-10, Pergamon Press, p. 1041, 1984.
 25. Bammann, D. J., Johnson, G. C., and Chiesa, M. L., “A Strain Rate Dependent Flow Surface Model of Plasticity”, SAND90-8227, 1990.
 26. Bammann, D. J., Chiesa, M. L., Horstemeyer, M. F., and Weingarten, L., “Failure in Ductile Materials Using Finite Element Methods”, in Structural Crashworthiness and Failure, Jones, N. and Wierzbicki, T. eds, Elsevier Science Publishers, 1993.
 27. Bammann, D. J., Chiesa, M. L., and Johnson, G. C., “Modeling Large Deformation and Failure in Manufacturing Processes”, to appear in ICTAM 96 conference proceedings, Kyoto, Japan, Aug. 1996.
 28. Lathrop, J. F., “BFIT - A Program to Analyze and Fit the BCJ Model Parameters to Experimental Data - Tutorial and User’s Guide”, Sandia Report SAND97-8281, Sandia National Laboratories, CA, December 1996.
 29. Mosher, D., “Elevated Temperature Notched Tensile Testing of 6061 Aluminum for FY96 DPTB Damage and Failure, Case #7164.230”, Internal Memo, Sandia National Laboratories, Livermore, CA, Oct. 1996.
 30. Forest, B., and Bercovici, S., “Experimental Study of Mechanical Properties of Aluminum Alloys during Controlled Solidification: Application to Hot Tearing”, Solidification Technology in the Foundry and Cast House, Coventry, Great Britain, Sept, pp. 607-612, 1980.
 31. Matsuda, F., Nakagawa, H., and Sorado, K., “Dynamic Observation of Solidification and Solidification Cracking during Welding with Optical Microscope (I) - Solidification Front and Behavior of Cracking”, 1982, Trans. JWRI, 11 (2), 67-77.
 32. Tallon, J. L., and Wolfenden, A., “Temperature Dependence of the Elastic Constants of Aluminum”, J. Phys. Chem. Solids, Vol. 40, pp. 831-837, 1979.
 33. Biffle, J. H., “JAC3D - A Three-Dimensional Finite Element Computer Program for the Nonlinear Quasistatic Response of Solids with the Conjugate Gradient Method”, Sandia Report SAND87-1305, Albuquerque, NM, 1993.
 34. Blanford, M. L., “JAS3D - A Multi-Strategy Iterative Code for Solid Mechanics Analysis, User’s Instructions, Release 1.4, Internal Sandia Document, December, 1996.
 35. Nedreberg, M. L., “Thermal Stress and Hot Tearing during the DC Casting of Al-Mg-Si Billets”, Ph.D. Dissertation, University of Oslo, 1991.

Figures

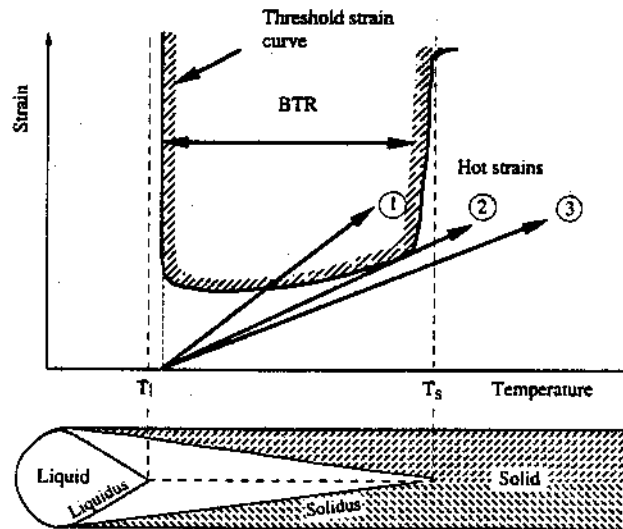
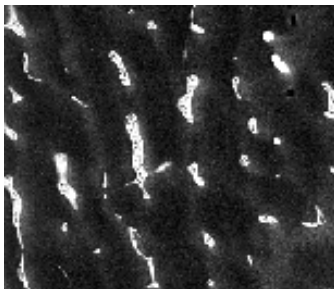
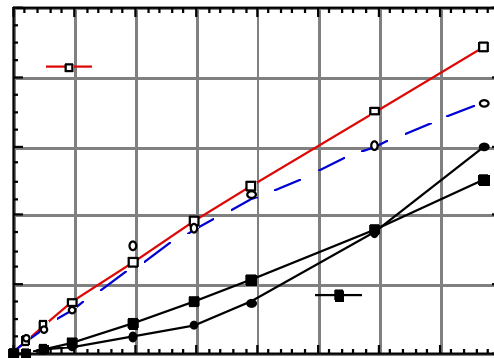


Figure 1. Schematic illustrating concept of hot strain during weld solidification versus material threshold strain for predicting solidification cracking from Matsuda, et. al.(2). Case (1) cracking, (2) marginal, (3) no cracking.



(a)



(b)

Figure 2. (a) SEM microstructure of Al-Cu weld showing eutectic solidification product θ (CuAl_2) in interdendritic regions. (b) Measured and calculated dendrite core concentration and volume fraction of θ , in Al-Cu welds made at 12.7 mm/s.

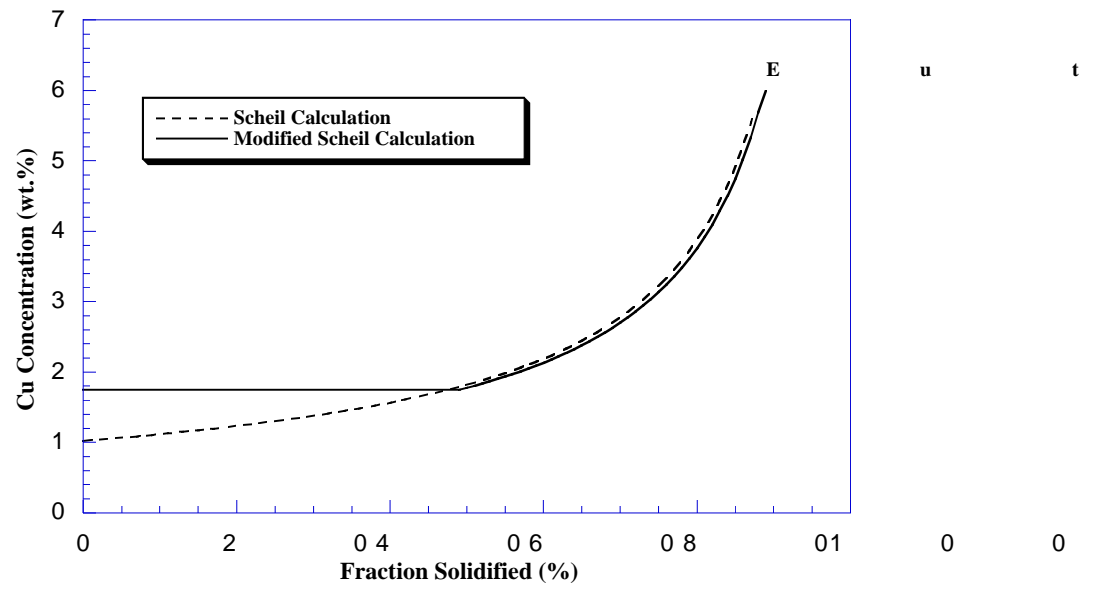


Figure 3. Predicted solidification behavior of Al- 5.93% Cu shown as concentration of solid vs fraction solidified.

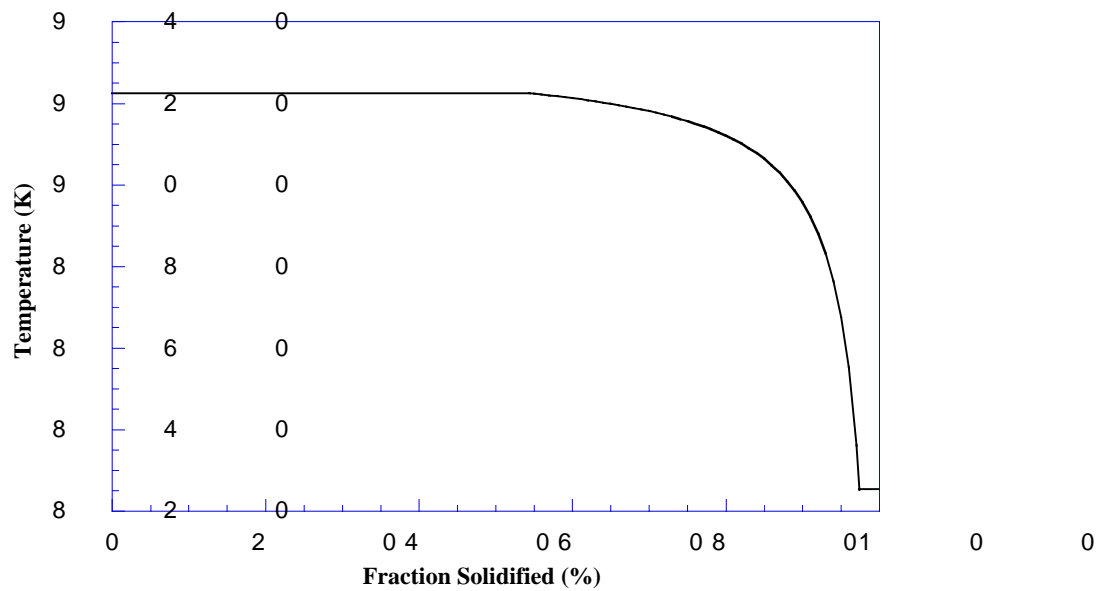
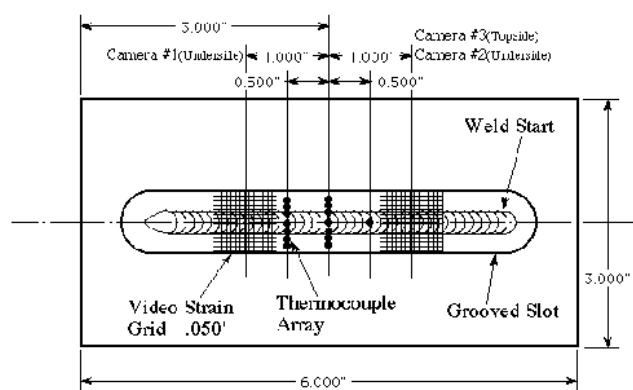


Figure 4. Fraction solid vs temperature for 6061 weld for solidification rate of 12.7 mm/s.



(a)



(b)

Figure 5. Cracking specimens used for thermal/mechanical code validation (a) and cracking studies (b).

(a)

(b)

Figure 6. Video images from underside of weld specimen. (a) weld coming into view at LHS (b) image taken after weld has passed. Strains are measured along position indicated.

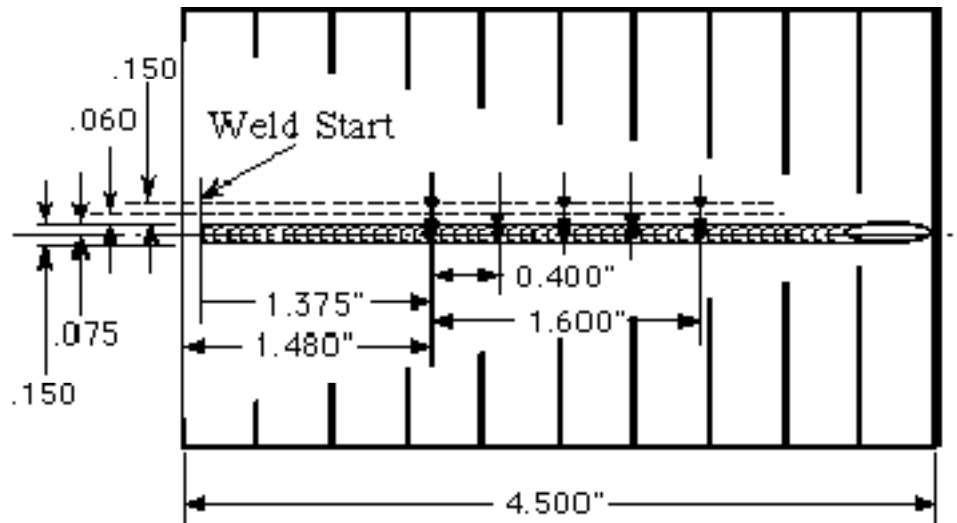


Figure 7. Schematic of Houldcroft solidification cracking specimen made from 0.050 inch thick sheet. Also noted on specimen is location of thermocouple placements.

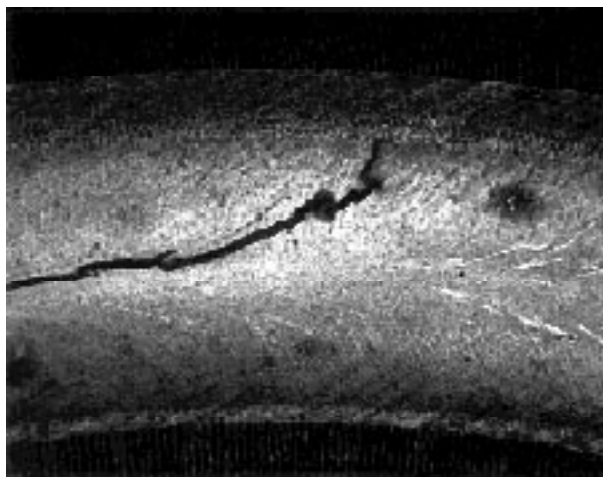


Figure 8. Solidification in weld cracking specimen in 6061. Note how crack initiates at outer edge of the fusion zone. Weld travels from right to left.

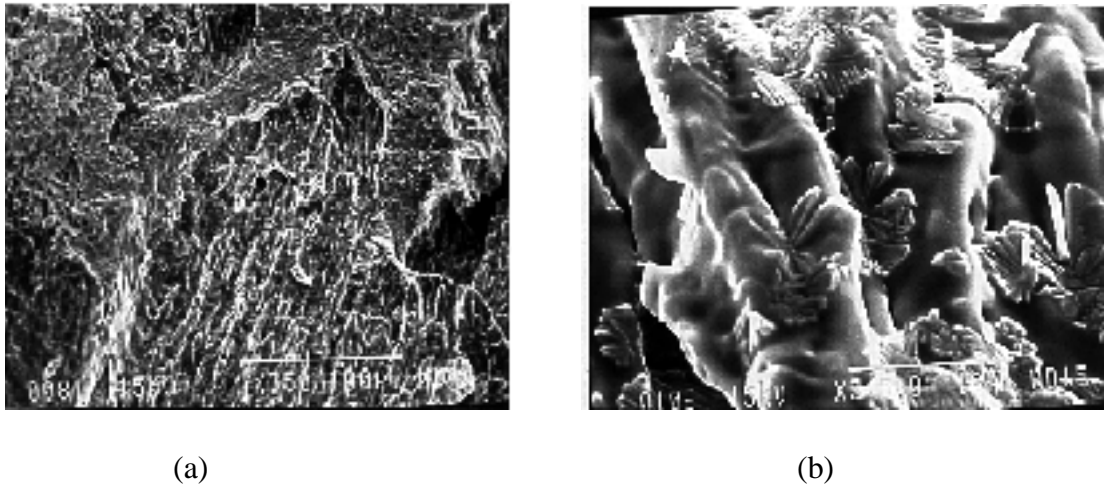


Figure 9. (a) SEM image of region of solidification crack initiation, (b) higher magnification of crack surface showing eutectic solidification products.

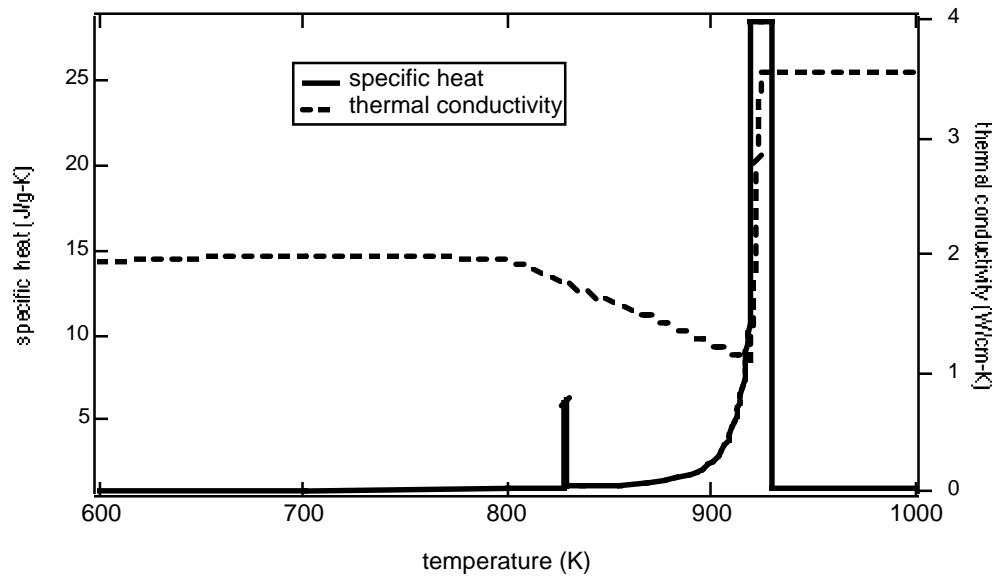


Figure 10. Properties used in thermal finite element analyses.

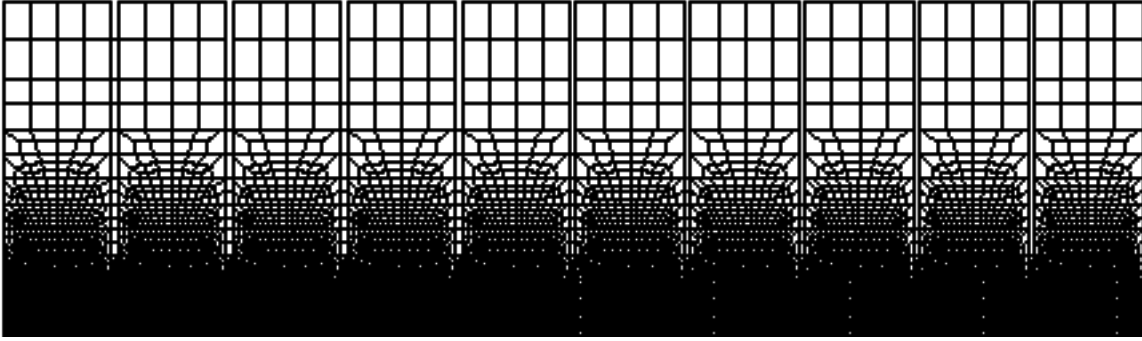


Figure 11. Finite element mesh used in Houldcroft analyses.

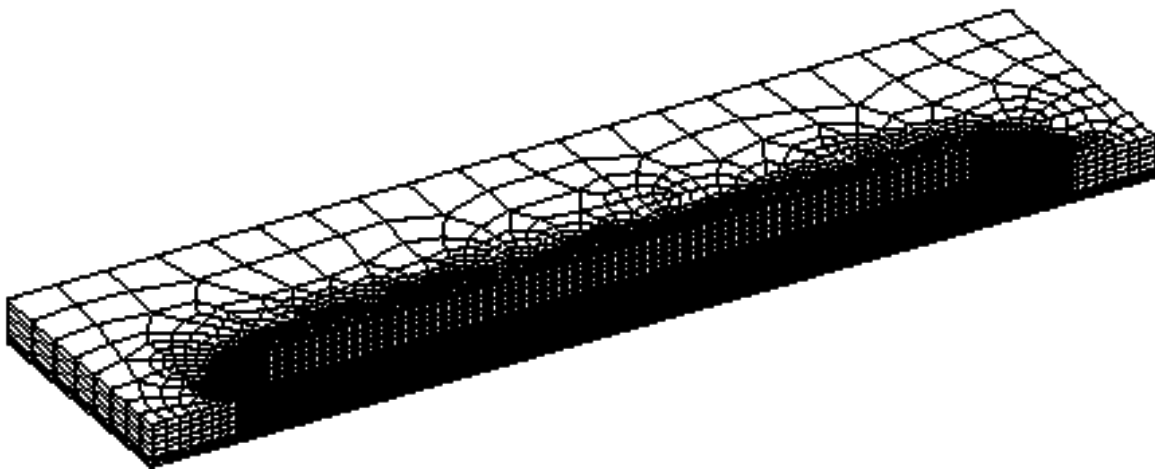


Figure 12. Finite element mesh used in analyses of 3"x6" slotted plates.

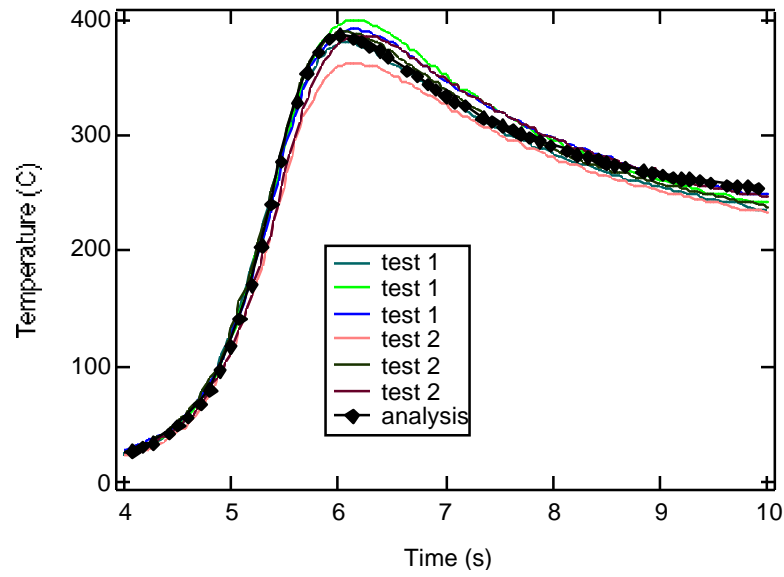


Figure 13. Temperature comparison between analysis and experiment for Houldcroft specimen, 5.7 mm from weld centerline.

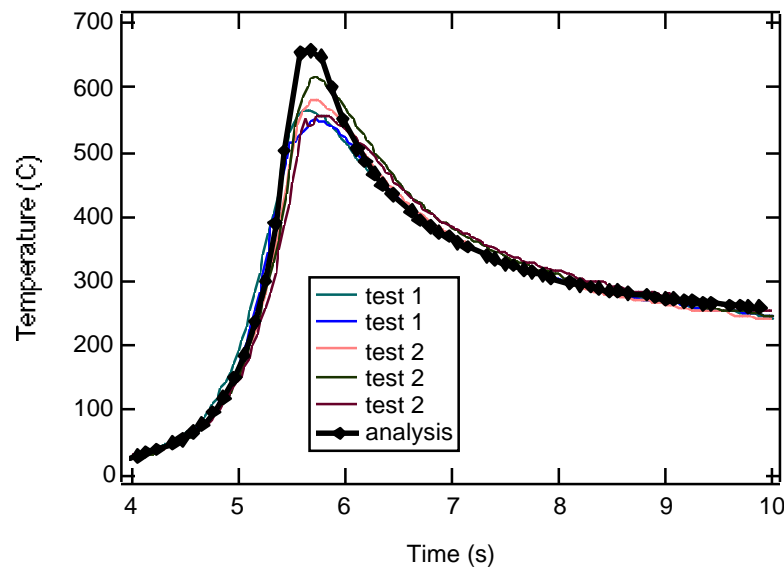


Figure 14. Temperature comparison between analysis and experiment for Houldcroft specimen, 1.7 mm from weld centerline.

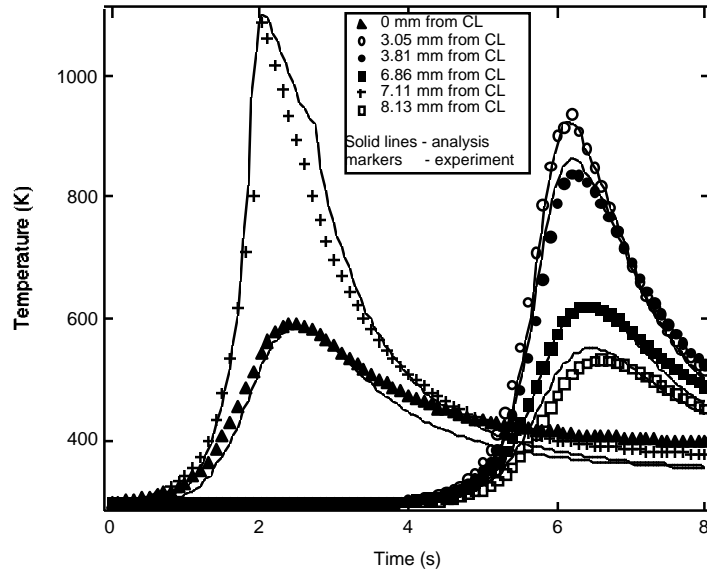


Figure 15. Comparison of temperature histories for 55 A, 17 V, 12.7 mm/s GTA weld. CL refers to the weld centerline.

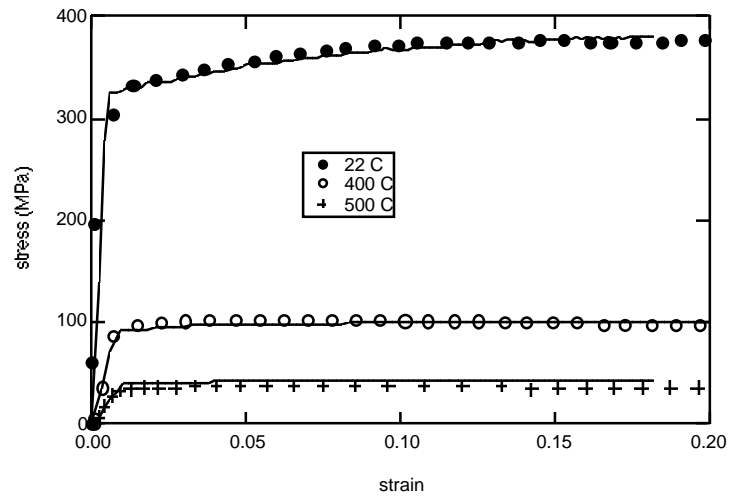


Figure 16. Comparison of BCJ fit with data from (29). Strain rate 0.2 s^{-1} .

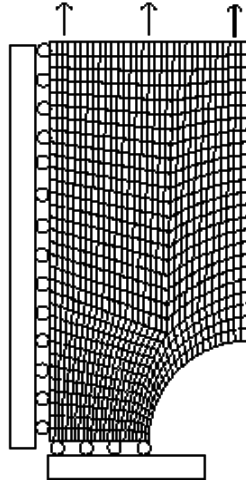


Figure 17. Axisymmetric finite element mesh and boundary conditions used to determine damage exponent for elevated temperature notched tensile tests.

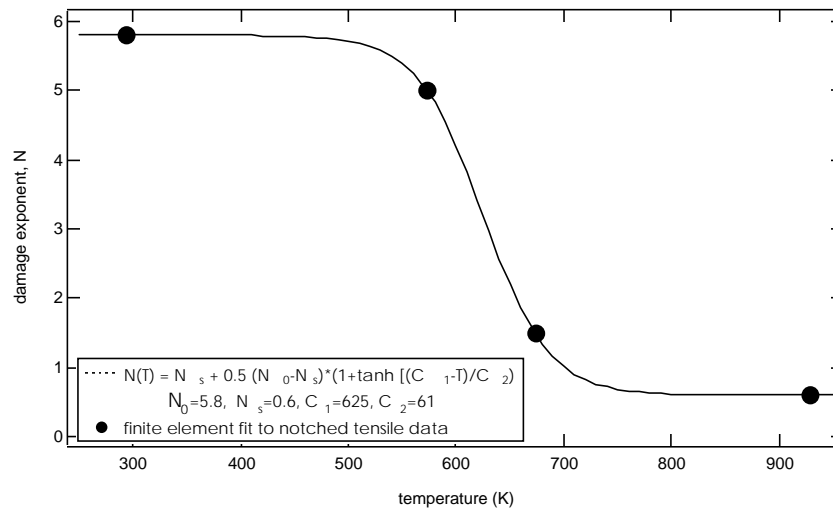


Figure 18. Temperature dependence of damage exponent n in Equation 2 as determined by finite element fits to elevated temperature notched tensile tests.

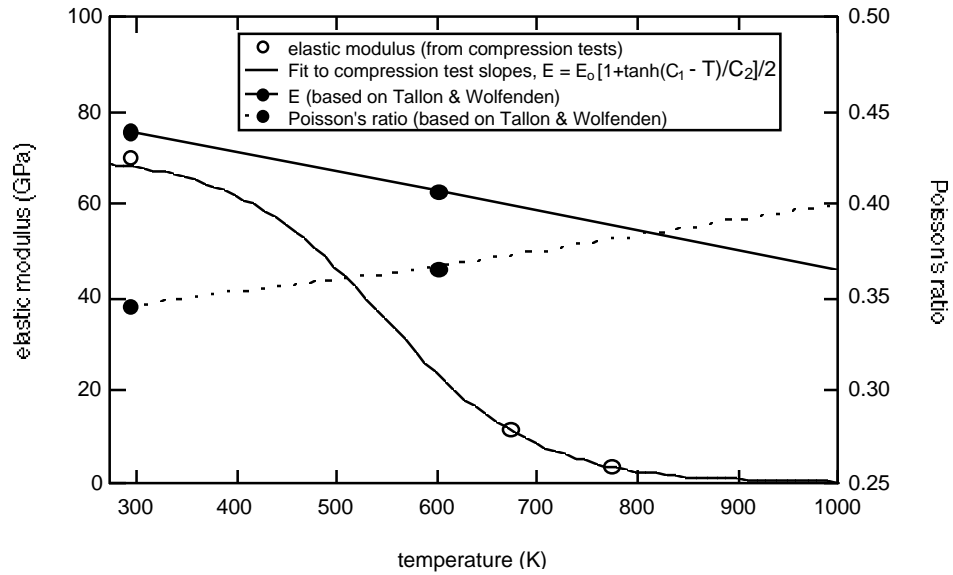


Figure 19. Temperature dependence of elastic constants used in mechanical analyses.

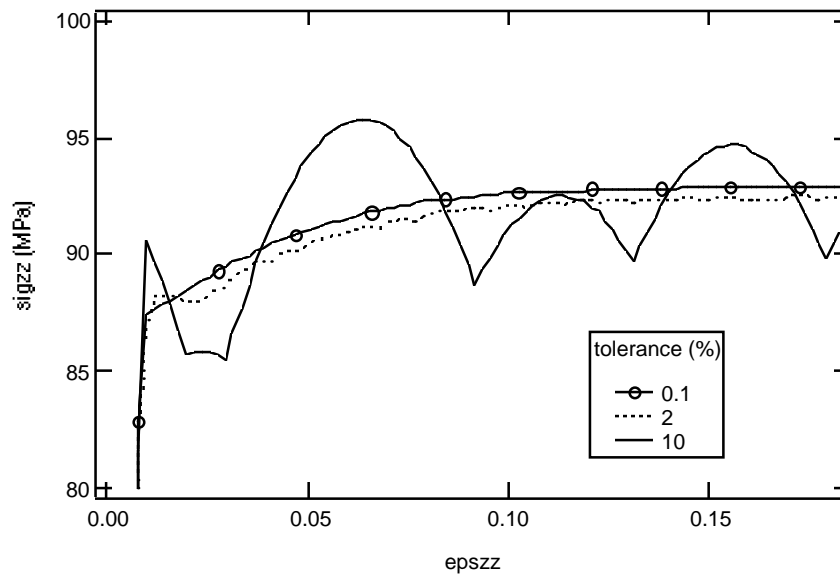


Figure 20. Stress-strain response for one-element mechanical analyses as a function of convergence tolerance at 400 C. 0.1%, 2%, and 10% tolerances.

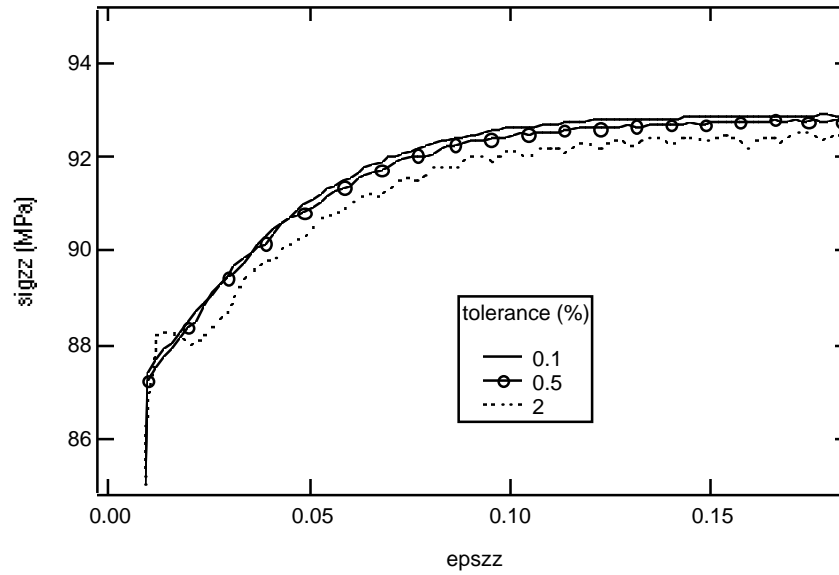


Figure 21. Stress-strain response for one-element mechanical analyses as a function of convergence tolerance at 400 C. 0.1%, 0.5%, and 2% tolerances.

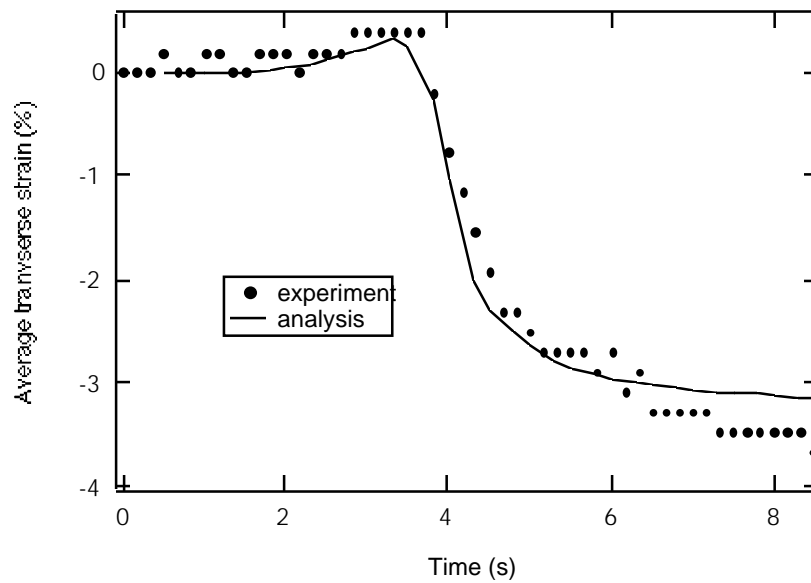


Figure 22. Comparison of transverse strains averaged across 6.35 mm weld for 6061-T6 Houldcroft specimen. Process parameters 40 A, 17V, 12.7 mm/s.

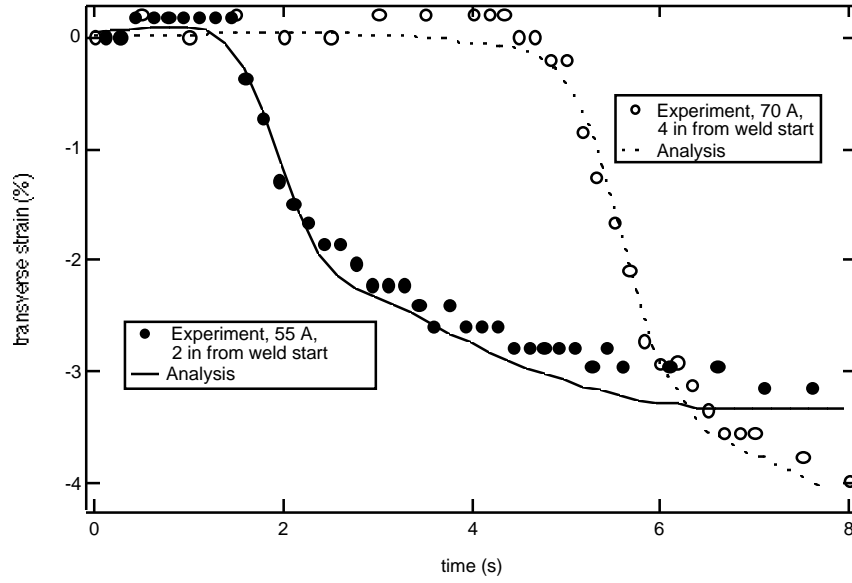


Figure 23. Comparison of transverse strains averaged across 6.35 mm weld for 3"x6" slotted 6061-T6 specimen. Process parameters are 55A and 70A, 17V, 12.7 mm/s.

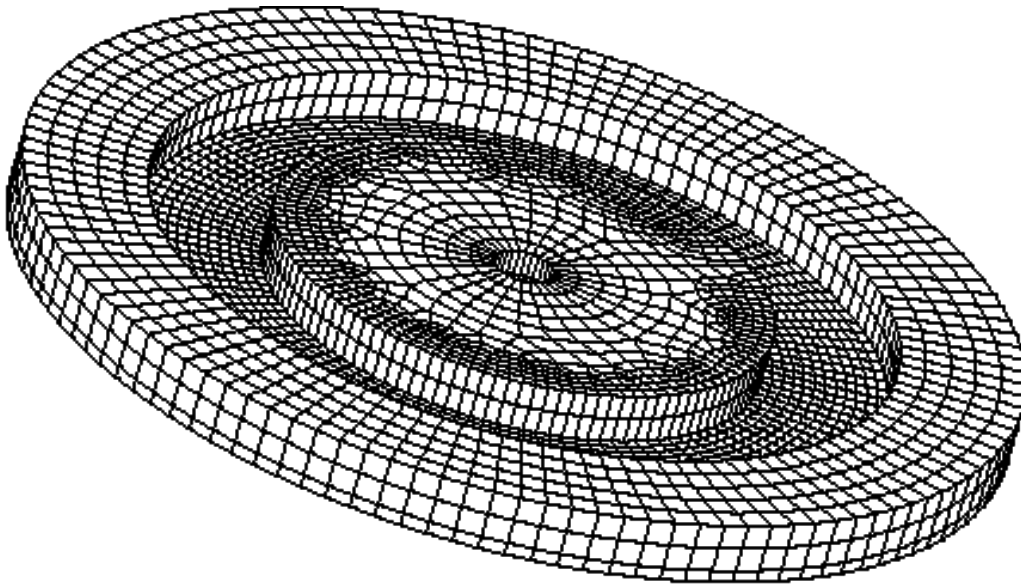


Figure 24. Sample of disk specimen finite element model.

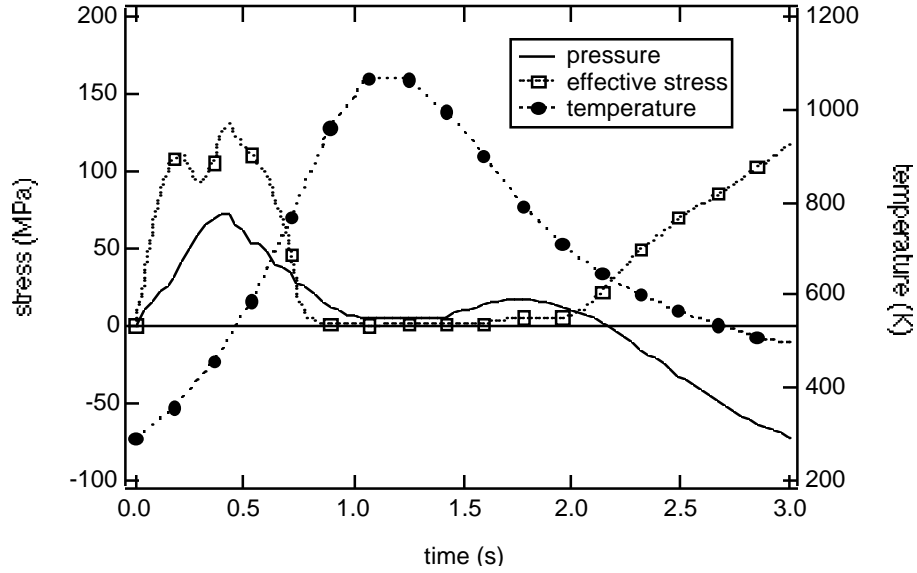


Figure 25. Pressure, effective stress, and temperature as a function of time for an element at center of weld in disk specimen for modulus fit to compression data.

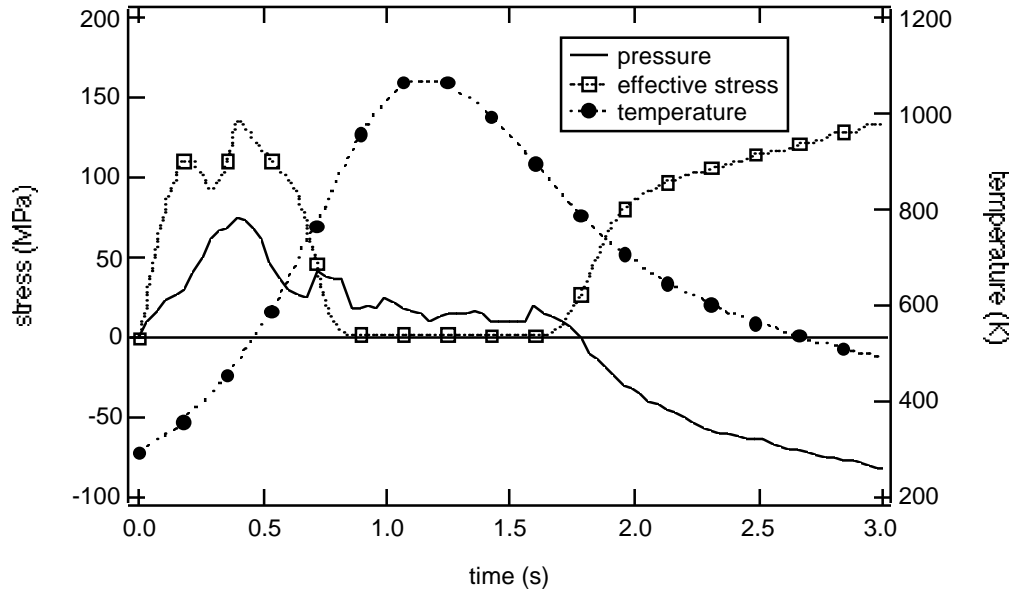


Figure 26. Pressure, effective stress, and temperature as a function of time for an element at center of weld in disk specimen for single crystal elastic constants (32).

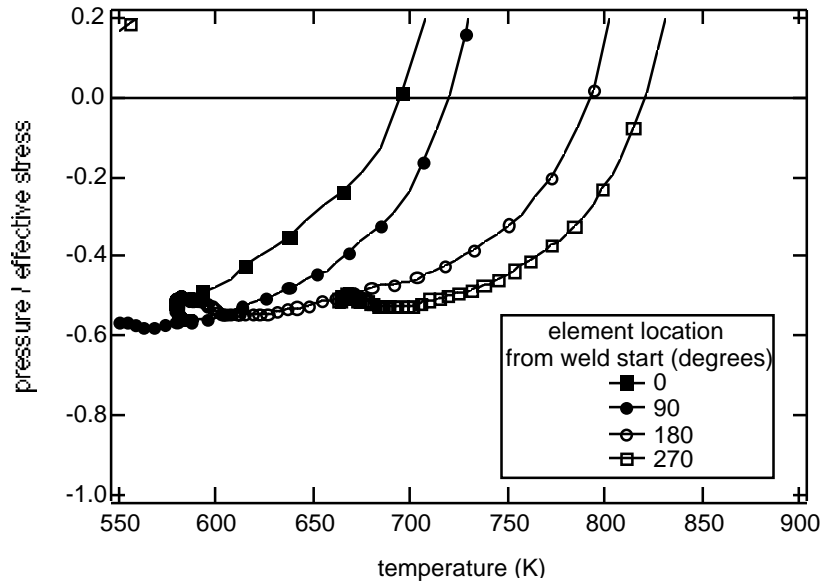


Figure 27. Temperature at which pressure becomes tensile (<0) as a function of distance from weld start for disk specimen.

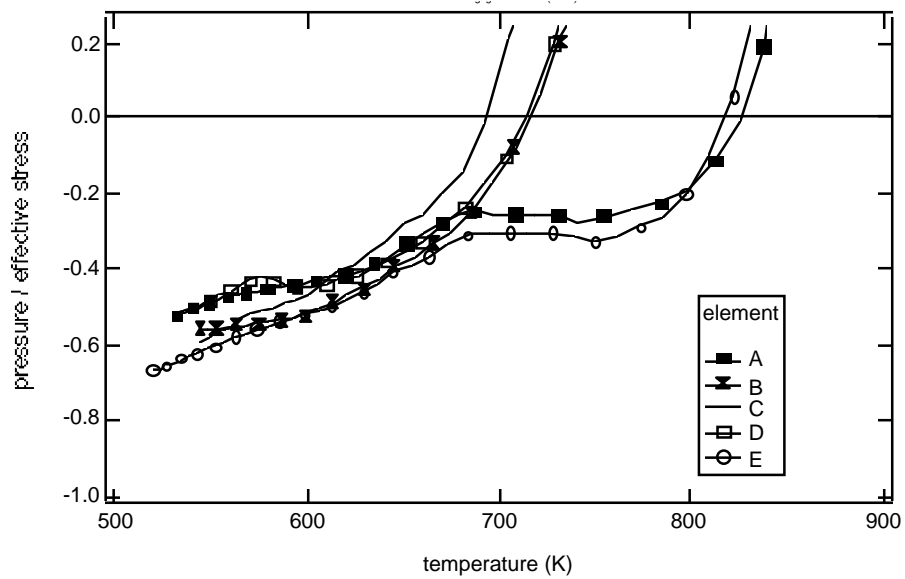


Figure 28. Temperature at which pressure becomes tensile (<0) for elements spanning the weld near weld start for the disk specimen.

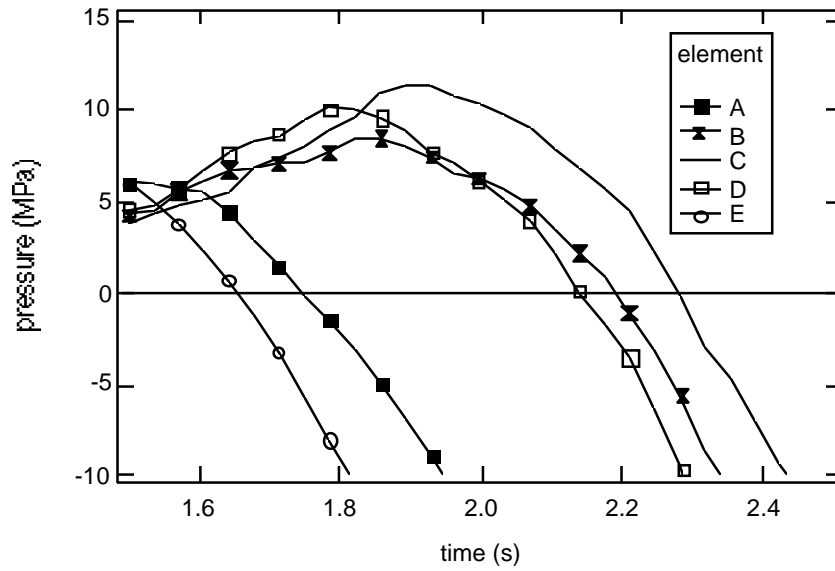


Figure 29. Time histories of pressure for elements spanning weld near weld start.

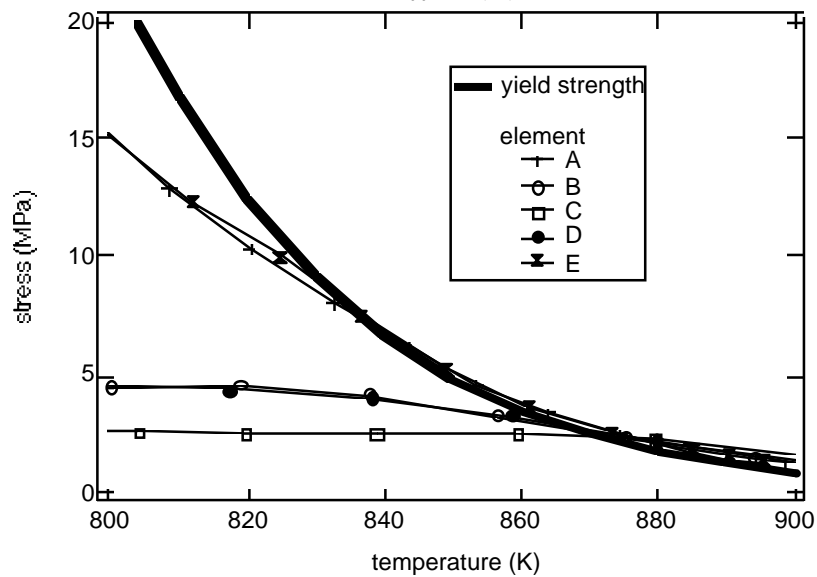


Figure 30. Effective stress as a function of temperature for elements spanning weld near weld start compared to yield stress as a function of temperature.

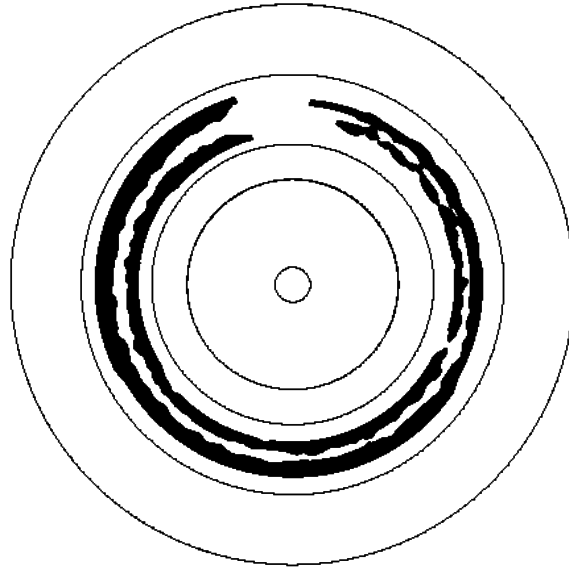


Figure 31. Calculated cracking for test 1. Welds start at top of disk and proceed clockwise. Dark areas show failed elements.

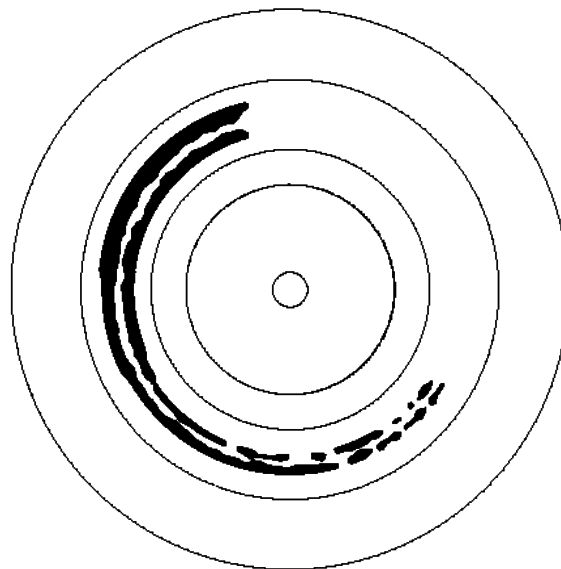


Figure 32. Calculated cracking for test 2, where cracking began near 190_ in the experiment.

Appendix A. Overview of the Bammann-Chiesa-Johnson Model

MODEL DESCRIPTION

The model used in this analysis was developed utilizing a multiplicative decomposition of the deformation gradient into elastic and plastic parts (details of the development are given in [A1]). The model is a strain rate and temperature dependent elastic-plastic model which uses internal variables which are introduced with respect to the unloaded configuration to describe the state of the material[A1,A2,A3,A4]. The stress is defined as the derivative of the free energy (in the stress free or intermediate configuration) with respect to the elastic strain in that same configuration. Assuming small elastic strains, taking the material derivative of the resulting Hooke's law and mapping forward to the current configuration results in the following,

$$\dot{\boldsymbol{\sigma}} - \mathbf{W}_e \boldsymbol{\sigma} + \boldsymbol{\sigma} \mathbf{W}_e \approx \lambda(1-\phi) \text{tr} \mathbf{D}_e \mathbf{I} + 2\mu(1-\phi) \mathbf{D}_e \quad (1)$$

where $\boldsymbol{\sigma}$ is the Cauchy stress, λ and μ are Lamé's constants, ϕ is the damage variable, and \mathbf{D}_e and \mathbf{W}_e are the elastic stretching and spin respectively. The elastic stretching is decomposed into total, plastic, volumetric, and thermal parts, while the elastic spin is defined as the difference between the total spin and plastic spin,

$$\mathbf{D}_e = \mathbf{D} - \mathbf{D}_p - \mathbf{D}_v - \mathbf{D}_{th}, \quad \mathbf{W}_e = \mathbf{W} - \mathbf{W}_p. \quad (2)$$

The plastic flow rule is chosen to have a strong nonlinear dependence upon the deviatoric stress $\boldsymbol{\sigma}'$,

$$\mathbf{D}_p = f(T) \sinh \left\{ \frac{|\boldsymbol{\sigma}' - \boldsymbol{\alpha}| - (\kappa - Y(T))(1 - \phi)}{V(T)} \right\} \frac{\boldsymbol{\sigma}' - \boldsymbol{\alpha}}{|\boldsymbol{\sigma}' - \boldsymbol{\alpha}|} \quad (3)$$

where $f(\theta)$ and $V(\theta)$ describe a rate dependence of the yield stress at constant temperature θ . The damage ϕ tends to concentrate the stress in the flow rule.

A tensor variable $\boldsymbol{\alpha}$ and a scalar variable κ have been introduced to describe the deformed state of the material. The evolution of both state variables is cast into a hardening minus recovery format. Both dynamic and thermal recovery terms are included. The dynamic recovery is motivated from dislocation cross slip that operates on the same time scale as dislocation glide. For this reason, no additional rate dependence results from this recovery term. The thermal recovery term is related to the diffusional process of vacancy assisted climb. Because this process operates on a much slower time scale, a strong rate dependence is predicted at higher temperatures where this term becomes dominant. The evolution for these variables is defined by

$$\dot{\kappa} = H(T) \mathbf{D}_p - \{R_s(T) + R_d(T) |\mathbf{D}_p|\} \kappa / \kappa, \quad (4)$$

$$\dot{\alpha} - \mathbf{W}_e \alpha + \alpha \mathbf{W}_e = h(T) \mathbf{D}_p - \{r_s(T) + r_d(T) |\mathbf{D}_p|\} \alpha / \alpha. \quad (5)$$

The tensor variable, α , represents a short transient and results in a smoother "knee" in the transition from elastic to elastic-plastic response in a uniaxial stress-strain curve. More importantly, this variable controls the unloading response and is critical in welding or quenching problems during the cooling cycle of the problem. It is termed a "short transient" in that it hardens rapidly and then saturates to a constant steady state value over a very short period of time during a monotonic loading at constant temperature and strain rate. This saturation value is maintained until the rate, temperature or loading path changes and the process repeats. This variable is responsible for the apparent material softening upon reverse loading termed the Bauschinger effect.

The scalar variable, κ , is an isotropic hardening variable that predicts no change in flow stress upon reverse loading. This variable captures long transients and is responsible for the prediction of continued hardening at large strains. Unlike α , once steady state has been reached under constant conditions, this variable is not affected by a change in loading, though it is still affected by changes in temperature.

The evolution of the damage state variable is based on the Cocks-Ashby model of growth of a spherical void in a rate dependent plastic material [A5]. The effects of damage due to the growth of an initial distribution of voids or initial porosity is modeled by the introduction of a scalar internal state variable ϕ . The variable acts to degrade the elastic moduli and concentrate the stress in the deviatoric flow rule. When damage reaches a critical value, failure occurs.

The evolution of the damage parameter ϕ , is given by

$$\dot{\phi} = \sinh\left(\frac{p}{|\sigma - \alpha|}\right) \left[\frac{1}{(1 - \phi)^n} - (1 - \phi) \right] |\mathbf{D}_p| \quad (6)$$

where $|\mathbf{D}_p|$ is the magnitude of the deviatoric plastic stretching and p is the tensile pressure.

While the system of equations (1) - (6), appear quite complex, much insight can be gained about each particular model parameter for a special set of loading conditions. Consider the case of uniaxial stress at constant true strain rate and temperature along with the viscoplastic assumption that at large strains the total strain rate and the plastic strain rate are essentially the same. We will also assume that the effects of void growth are negligible for this case as long as we restrict our attention to strains below barreling or necking. For this case, equations (4) and (5) can be integrated analytically to yield,

$$\alpha = \sqrt{\frac{h\dot{\epsilon}}{r_d\dot{\epsilon}+r_s}} \tanh \left\{ \sqrt{\frac{h(r_d\dot{\epsilon}+r_s)}{\dot{\epsilon}}} \epsilon \right\} \quad (7)$$

$$\kappa = \sqrt{\frac{H\dot{\epsilon}}{R_d\dot{\epsilon}+R_s}} \tanh \left\{ \sqrt{\frac{H\dot{\epsilon}(R_d\dot{\epsilon}+R_s)}{\dot{\epsilon}}} \epsilon \right\} \quad (8)$$

Then by taking the magnitude of each side of equation (2) for the flow rule and inverting, we can write the flow stress as,

$$\sigma = \alpha + \kappa + Y(\theta) + V(\theta) \sinh^{-1} \left\{ \frac{|\dot{\epsilon}|}{f(\theta)} \right\} \quad (9)$$

where, σ and ϵ are the true stress and true strain in uniaxial tension or compression. Using equations (7-9) we can now utilize tension or compression data at different strain rates and temperatures along with a nonlinear regression analysis.

REFERENCES

- A1. D. J. Bammann, "An Internal Variable Model of Viscoplasticity," *Int. J. Eng. Sci.*, 22 (1984), pp. 1041-1053.
- A2. D. J. Bammann, "Modeling Temperature and Strain Rate Dependent Large Deformations of Metals," *Appl. Mech. Rev.*, 1 (1990), 312-318.
- A3. D. J. Bammann and G. C. Johnson, "On the Kinematics of Finite Deformation Plasticity", *Acta Mechanica*, 70 (1987), pp. 1-13.
- A4. D. J. Bammann and E. C. Aifantis, "A Model for Finite Deformation Plasticity", *Acta Mechanica*, 69 (1987), pp. 97-117.
- A5. Cocks, C. F., and Ashby, M. G., "Intergranular Fracture During Power Law Creep Under Multiaxial Stresses", *Metal Science*, Aug-Sept, pp. 395-402, 1980.

Appendix B. Two phase (Solid-Liquid) form of the Bammann-Chiesa-Johnson Model

We begin by assuming that each point can be occupied simultaneously by both solid and liquid phases. Then the total stretching can be partitioned into the stretching in each phase as,

$$D = D_L (1 - f) + f D_S \quad (1)$$

where f is the volume fraction of solid, and subscripts “L” and “S” denote liquid and solid respectively. Similarly, the stresses are assumed to partition according to a rule of mixtures as

$$\sigma = \sigma_L (1 - f) + f \sigma_S \quad (2)$$

In this approach the strain rates in each phase will be determined from self consistent techniques. Initially we will make a Taylor assumption, that is the strain rate is partitioned equally in all phases. To account for the inaccuracies in this assumption, we will modify the rule of mixtures associated with the stresses,

$$\sigma = \sigma_L (1 - \hat{f}) + \hat{f} \sigma_S \quad (3)$$

where, \hat{f} is a user chosen parameter to reduce the inaccuracies associated with the Taylor assumption. In particular,

$$\hat{f} = \left(1 - \tanh \left[\frac{(CC1 - f)}{CC2} \right] \right) \quad (4)$$

This partitions most of the stress into the liquid until a critical volume fraction of solid (CC1) is reached. At this point, the solid will carry most of the stress with the rate of stress redistribution controlled by the constant CC2.

Having made these assumptions, we will model the solid phase using the BCJ model described in Appendix A, with additional modifications to the damage evolution to account for nucleation in the liquid phase. We begin by assuming that the damage is the product of the total number of voids per unit volume, N , and the average void volume size, V . Then, the time rate of change of the damage is given as,

$$\dot{\phi} = \dot{N}V + N\dot{V} \quad (5)$$

The evolution of the void growth is as before,

$$\dot{V} = \left(\frac{1}{(1-\phi)^n} - (1-\phi) \right) \sinh \left(\frac{p}{\sigma} \right) |D_p| \quad (6)$$

The nucleation will be chosen to represent void nucleation at the liquid-solid interface in the simplest possible form. More physics of the process will be given in a future article. Initially, we choose for the nucleation the form,

$$\dot{N} = (1-\phi) \left\langle \left(\text{tr}(\mathbf{D}) - \frac{p^{\text{critical}}}{CC3} \right) \right\rangle \quad (7)$$

where CC3 is a constant related to void nucleation. For the deviatoric stresses in the liquid phase we assume a viscous fluid,

$$\boldsymbol{\sigma}' = \mu \mathbf{D}' \quad (9)$$

where, μ is the viscosity. For the mean stress in the fluid we will assume an elastic response,

$$\dot{p} = K \text{tr}(\mathbf{D}) \quad (10)$$

where, K, is the bulk modulus of the liquid. Any volumetric strain associated with the nucleation of voids in the liquid solid interface will be neglected as a first approximation.

UNLIMITED RELEASE

INITIAL DISTRIBUTION:

MS0367	B. K. Damkroger, 1833
MS1436	C. Meyers, 4523
MS9001	T. O. Hunter, 8000
	Attn: P. N. Smith, 8500, MS9002
	D. L. Crawford, 8900, MS9003
	M. E. John, 8100, MS9004
	J. B. Wright, 2200, MS9005
	R. C. Wayne, 8400, MS9007
	W. J. McLean, 8300, MS9054
	P. E. Brewer, 8800, MS9141
MS9402	M. I. Baskes, 8712
MS9402	G. J. Thomas, 8715
MS9402	N. Y. C. Yang, 8715
MS9405	T. M. Dyer, 8700
	Attn: M. W. Perra, 8711, MS9402
	J. C. F. Wang, 8713, MS9403
	K. L. Wilson, 8716, MS9161
	W. G. Wolfer, 8717, MS9161
	M. R. Birnbaum, 8742, MS9042
	W. A. Kawahara, 8746, MS9042
MS9405	D. J. Bammann, 8743
MS9405	P. E. Nielan, 8743
MS9420	A. J. West, 8240
	Attn: L. N. Tallerico, 8204, MS9430
	M. H. Rogers, 8220, MS9420
	J. M. Hruby, 8230, MS9405
	R. H. Stulen, 8250, MS9409
	V. C. Barr, 8250-1, MS9107
MS9430	C. H. Cadden, 8240
MS9430	J. A. Brooks, 8240 (5)
MS9430	J. Krafcik, 8240
MS9430	M. Li, 8240
MS9042	J. J. Dike, 8743 (5)
MS9042	M. F. Horstemeyer, 8743
MS9042	A.R. Ortega, 8743
MS9042	M. Kanouff, 8743
MS 9021	Technical Communications Department, 8815/Technical Library, MS 0899, 4414
MS 9021	Technical Communications Department 8815, for OSTI (10)
MS 0899	Technical Library, 4414 (4)
MS 9018	Central Technical Files, 8940-2 (3)